Structure, signals, and cellular elements of the mouse gastric mesenchymal niche

Elisa Manieri[1,2], Guodong Tie[1], Davide Seruggia[3,4], Shariq Madha[1], Adrianna Maglieri[1], Kun Huang[6], Yuko Fujiwara[3], Kevin Zhang[3], Stuart Orkin[3,7,8], Ruiyang He[1,2], Neil McCarthy[1,2], Ramesh A. Shivdasani[1,2,8,*]

[1]Department of Medical Oncology and Center for Functional Cancer Epigenetics, Dana-Farber Cancer Institute, Boston, MA 02215, USA; [2]Departments of Medicine, Brigham & Women's Hospital and Harvard Medical School, Boston, MA 02115, USA; [3]Department of Hematology, Boston Children's Hospital, Boston, MA 02115, USA; [4]St. Anna Children's Cancer Research Institute, Vienna, Austria; [5]CeMM Research Center for Molecular Medicine of the Austrian Academy of Sciences, Vienna, Austria; [6]Department of Cancer Immunology, Dana-Farber Cancer Institute, Boston, MA 02215, USA; [7]Howard Hughes Medical Institute, Boston, MA 02115, USA; [8]Harvard Stem Cell Institute, Cambridge, MA 02138, USA.

*Corresponding author and Lead Contact: Ramesh A. Shivdasani, MD, PhD
Dana-Farber Cancer Institute
450 Brookline Avenue, Boston, MA 02215, USA
ramesh_shivdasani@dfci.harvard.edu

SUMMARY

PDGFRA-expressing mesenchymal cells provide a crucial niche for the self-renewing intestinal epithelium. Corresponding compartments remain unclear in the stomach, where corpus and antral glandular epithelia have similar niche dependencies but are structurally distinct from the intestine and from each other. Previous studies considered antrum and corpus as a whole and did not assess niche functions. We applied high-resolution approaches to identify regional subpopulations and niche properties of purified corpus and antral PDGFRA^{+} cells. PDGFRA^{Hi} sub-epithelial myofibroblasts are the principal sources of BMP ligands in both gastric segments, fall into two molecularly distinct groups that distribute asymmetrically along antral glands, and fail to support epithelial organoids *in vitro*. In contrast, PDGFRA^{Lo} cells expressing CD55 from either segment uniquely enable corpus and antral organoid growth in the absence of other cellular or soluble factors. Our study provides detailed insights into spatial and functional organization of gastric mesenchyme and the spectrum of signaling sources.

INTRODUCTION

Balanced self-renewal and differentiation of digestive epithelia relies on interactions with the underlying mesenchyme; these interactions serve as a model for adult tissue homeostasis. Stomach and intestinal epithelia share essential features, including long-lived stem cells that generate a limited number of cell types within stereotypic monoclonal crypts (intestine) or glands (stomach), but their functions and stem cell kinetics differ. *Lgr5*-expressing intestinal stem cells (ISCs) at the base of each crypt drive brisk cell turnover, whereas the gastric corpus epithelium turns over slowly, fueled by stem cells of uncertain identity and unknown molecular markers in the isthmus of each glandular unit (Figure 1A). Antral epithelium bridges the corpus and intestine, lacks villi, turns over at an intermediate rate (Karam and Leblond, 1993a; Leushacke et al., 2013; Matsuo et al., 2017), and consists mainly of foveolar and mucous cells. Antral stem cells express *Lgr5* and concentrate near the gland base (Figure 1A). Recent studies have defined anatomic and functional relations between intestinal stromal and epithelial sub-compartments (Aoki et al., 2016; Degirmenci et al., 2018; Greicius et al., 2018; McCarthy et al., 2020; Shoshkes-Carmel et al., 2018). In contrast, gastric mesenchyme remains superficially characterized; a recent single-cell analysis combined corpus and antral cells, obscuring their individual properties (Kim et al., 2020). The dense stroma underlying corpus and antral epithelia contains blood vessels, smooth muscle, neuroglia, and poorly characterized “fibroblasts.” Here we report on our structural, molecular, and functional characterization of adult mouse corpus and antral mesenchyme at the level of whole tissues and single cells.

In the corpus, mucus-producing foveolar cells line a luminal “pit”; below the pit, the isthmus carries slow-cycling stem cells of uncertain identity and their transit-amplifying progeny, which produce various mature cell types (Figure 1A). The neck of each corpus gland carries mucous neck cells and acid-producing parietal cells, while pepsinogen-secreting chief cells populate the gland base. Corpus stem cell daughters migrate bidirectionally along the vertical gland axis, with foveolar precursors moving toward the pit and other precursors moving toward the gland base (Karam, 1993; Karam and Leblond, 1993b, c). In the antrum, proliferative epithelial cells reside in 3-4 cell tiers above the basal *Lgr5*$^{+}$ stem cell zone and their progeny mainly migrate upward to replenish the physiologic attrition of terminally differentiated foveolar and mucous cells (Barker et al., 2010) (Figure 1A). Antral stem cells require Wnt signaling to proliferate and maintain their identity (Barker et al., 2010; Sigal et al., 2017; Sigal et al., 2019), while bone morphogenetic protein (BMP) signaling drives epithelial differentiation (Kapalczynska et al., 2022; Shinohara et al., 2010; Wolffling et al., 2021) and its inhibition plays a role in gastric

metaplasia and *Helicobacter pylori* infection (Todisco, 2017; Ye et al., 2018). Here we define the relations between distinct digestive epithelia and their underlying stromal elements, revealing important functional differences between the small intestine, gastric corpus, and gastric antrum.

RESULTS

Anatomic definition and signaling potential of antrum and corpus mesenchyme

Foveolar cells are present in both gastric regions, with a larger fraction in the antrum, where pits (foveolae) are wider and deeper than those in the corpus (Figure S1A). In both regions, whole-mount confocal imaging revealed blood vessels and smooth muscle fibers packed tightly between glands (Figure 1B). Slender corpus arterioles branch along the full gland length to form a deep capillary network, while antral arterioles have a large bore and extend capillaries only at gland tops, with little branching along the gland length (Figures 1C and S1B). Smooth muscle fibers extend lateral branches near the foveolar base, so the resulting fine network of smooth muscle cells is taller and wider in the antrum (Figure 1C). *Pdgfra*-expressing mesenchymal cells are pivotal in intestinal epithelial homeostasis (McCarthy et al., 2020). In *Pdgfra*^{H2BeGFP} knock-in mice (Hamilton et al., 2003; Kurahashi et al., 2013), we detected cells with high and low levels of nuclear GFP (Figures 1D and S1C-E). Antral PDGFRA^{Hi} cells concentrate around the pit, where they extend beyond the basement membrane into the lamina propria, while corpus PDGFRA^{Hi} cells are found uniformly along corpus glands. PDGFRA^{Lo} cells distribute uniformly along the gland length in both segments and concentrate below the gland base, showing higher cell density in the corpus (Fig. S1E). To assess cell morphology more finely, we crossed *Pdgfra*$^{Cre(ER-T2)}$ knock-in mice (Chung et al., 2018) with the *Rosa26*$^{mT/mG}$ reporter strain (Muzumdar et al., 2007), thus producing mice where baseline red fluorescence (tomato) in all cell membranes changes to green (GFP) in cells with Cre enzyme activity. PDGFRA^{Hi} cells embedded in the basal lamina engulf each gland within their cytoplasmic extensions (Figures 1E and S1F). Thus, submucosal cell arrangements vary along the digestive tract, especially among *Pdgfra*-expressing mesenchymal cells, likely reflecting distinct influences on regional epithelia. (Figure 1F).

SI crypts form organoid structures in Matrigel supplemented with EGF, Noggin (a BMP inhibitor), and RSPO1, a Wnt potentiating agent (ENR medium) (Sato et al., 2009). As *Lgr5*$^{+}$ stem cells in the antral gland base resemble those in intestinal crypt bottoms, conditions to culture antral organoids were adapted from this foundation and include a requirement for Wnt3a

in addition (ENRW) (Barker et al., 2010). Selected intestinal PDGFRA^{Lo} cells, which express BMP inhibitor (BMPi) and RSPO genes, induce intestinal crypts to form spheroids *in vitro* in the absence of any supplemental factors (McCarthy et al., 2020). PDGFRA^{Lo} cells isolated by flow cytometry from each gastric segment (Figure S1G) also induced spheroids when co-cultured, without recombinant (r) factors, with glands from the same region (Fig. S1H); however, PDGFRA^{Lo} cells sorted from the gastric corpus or antrum failed to support intestinal crypts *in vitro* (Figures 1G and S1I). Thus, gastric and intestinal stem cells have distinct cellular support requirements and PDGFRA^{Lo} cells in each mesenchyme support homologous epithelial stem cells better than heterologous stem cells.

Regionality of gastrointestinal Pdgfra-expressing mesenchymal cells

To identify the mesenchymal basis of gastric epithelial support, we aimed first to refine factor requirements for organoid growth, deploying culture conditions that avoid carry-over of fetal bovine serum (FBS) serum from any component. Organoids cultured in ENRW medium expressed site-specific transcripts (Figure S2A) and we examined changes in the numbers and size of antral and corpus organoids in response to modification of the culture medium. Corpus glands were more sensitive than antral glands to removal of any factor and, consistent with previous reports (Murakami et al., 2021), lack of Wnt3a or RSPO1 had the largest impact on organoid formation from both sites (Figure S2B). Compared to glands cultured in ENRW, organoid output was barely compromised from glands cultured without rEGF or rNoggin (Figure S2B). Cutting Wnt3a and RSPO1 supplementation in half reduced corpus organoid size modestly, while antral organoids were not adversely affected (Figure 2A). Organoids of reduced size grew from both sites in the absence of rEGF and corpus organoid size was more sensitive to rNoggin depletion than antral organoids; rEGF, but not rNoggin, improved antral organoid growth independent of Wnt3a or RSPO1. These findings reinforce Wnt, BMP, and EGF signaling requirements in gastric stem cell growth, reveal measurable specificity in each site, and imply that mesenchymal cell products may differ to match epithelial needs.

PDGFRA^{Hi} intestinal sub-epithelial myofibroblasts (ISEMFs) produce differentiation-inducing BMP ligands and sub-cryptal CD81^{+} PDGFRA^{Lo} “trophocytes” oppose that signal best to expand ISCs *in vitro* (McCarthy et al., 2020). Although stomach mesenchymal PDGFRA^{Lo} cells lack CD81 heterogeneity (as we show below by single-cell RNA-seq), segment-specific supportive activity of bulk PDGFRA^{Lo} cells (Figure 1G) implies that they provide certain key factors. To dissect regional mesenchymal differences, we profiled bulk transcriptomes of PDGFRA^{+} cells

purified by flow cytometry from the corpus and antrum of *Pdgfra*^{H2BeGFP} mice; by stripping away external muscle before cell purification, we excluded PDGFRA^{Hi} neurons nestled therein, so that remaining PDGFRA^{Hi} cells represent SEMFs. Replicate RNA-seq libraries from each cell isolation were highly concordant (Figure S2C). In unsupervised hierarchical analysis, the clearest distinction was between gastric PDGFRA^{+} cells and their previously described intestinal counterparts (McCarthy et al., 2020), followed by differences between PDGFRA^{Hi} and PDGFRA^{lo} cells in each organ (Figure 2B). Gastric corpus and antral PDGFRA^{Hi} cell (SEMF) transcriptomes largely resembled each other, compared to the substantial differences between SEMFs in the SI and those in either stomach segment (Figures 2C, S2D, and Table S1). Exclusive expression of known transcriptional regulators *Barx1* and *Pitx1* in gastric cells and of *Nkx2-3* and posterior *Hox* genes in intestinal cells support the veracity of additional findings, for example that gastric SEMFs express higher levels of *Fgf7* (a gene we examine later in this study), *Fbln1* and *Fbln2*, *Cd81*, and transcription factor genes *Atf3* and *Osr1*. Conversely, intestinal SEMFs express higher levels of *Il33* and *Il34*, the Wnt inhibitor *Wif1*, and transcription factor *Irf8* (Figures 2C, S2D, and Table S1). Significant differential expression of *Acta2* and *Myh11* suggests that intestinal and antral SEMFs are likely more contractile than their corpus counterparts (Figures 2C, S2D, and Table S1).

Segment- and cell type-specific gene modules were evident in each population, with certain elements, e.g., *Hox* genes, enriched as expected in both SEMFs and PDGFRA^{Lo} cells from any segment (Table S1). Intestinal PDGFRA^{Lo} cells have the most distinctive transcriptome of any population, with unique expression of *Eln*, *Col8a1*, and *Il6*, among other factors (Figures 2D, S2E, and Table S1). Where intestinal SEMFs and PDGFRA^{Lo} cells differ from each other at >2,400 genes, compatible with distinct and opposing functions (McCarthy et al., 2020), the corresponding populations in both stomach segments are less divergent, differing in expression of <900 (antrum) to <1,200 (corpus) genes (Figure S2G). Gastric PDGFRA^{Lo} cells from either segment are enriched for *Cd55* (a marker we investigate later in this study), *Lepr* and *C3* (genes that mark mesenchymal cells in mouse and human intestinal mesenchyme, respectively), while gastric SEMFs are enriched for signaling factors such as *Fgf9* and *Angptl1*, multiple BMP genes, and for transcription factor (TF) gene *Sox6* and, in the antrum, Wnt-responsive *Lef1* (Figures 2C-D, S2D, and Table S1). *Foxl1*, which marks intestinal SEMFs among other cells (Aoki et al., 2016; McCarthy et al., 2020; Shoshkes-Carmel et al., 2018), is expressed in gastric SEMFs and, at a lower level, also in gastric PDGFRA^{Lo} cells. Thus, regional differences in the spatial arrangements of *Pdgfra*-expressing cells extend to their gene expression profiles.

Among potential sources of the signals that support epithelial expansion *in vitro*, genes for canonical *Wnt2* and for non-canonical ligands *Wnt4*, *Wnt5a*, and *Wnt5b* are expressed in both PDGFRA^{+} populations in both stomach segments; however, Wnt-potentiating factors *Rspo1*, *Rspo2*, and *Rspo3* express at lower levels in gastric than in intestinal PDGFRA^{Lo} cells (Figure 2E). Thus, while PDGFRA^{+} cells in every segment produce Wnt ligands, only transcripts in intestinal PDGFRA^{Lo} cells display a potential for significant canonical Wnt signaling to the overlying epithelium. Notably, BMP transcripts are enriched not only in intestinal, antral, and corpus PDGFRA^{Hi} cells, but *Bmp2*, *Bmp5*, and *Bmp7* are also prominent in gastric PDGFRA^{Lo} cells (Figure 2E). BMP antagonist *Grem1*, abundant in intestinal PDGFRA^{Lo} cells, or other classical BMP antagonists are barely present in gastric PDGFRA^{Lo} cells, which instead express a putative and atypical BMP7 inhibitor, *Ctgf* (Abreu et al., 2002; Nguyen et al., 2008). Based on mRNA levels alone, these findings suggest that overall BMP "tone" may be higher in the stomach than in the small intestine.

Gastric organoids generally display spheroid morphology (see Figure 1G), distinct from intestinal organoids, in which budding protrusions represent crypts housing progenitor and stem cells (Sato et al., 2009). When culture conditions were first defined for antral organoid growth, addition of human fibroblast growth factor (FGF) 10 to the medium induced budding (Barker et al., 2010). Although the *in vivo* significance of this observation is unclear (glandular stomach epithelium lacks crypt structures), the asymmetry of FGF mRNA expression in PDGFRA^{+} cells is striking. Of the five transcripts expressed in any population, *Fgf9* is expressed in SEMFs and *Fgf10* in PDGFRA^{Lo} cells from all sites, while *Fgf7* is especially high in antral SEMFs. *Nrg1*, an EGF-family factor implicated in ISC regeneration after injury (Jarde et al., 2020), is also uniquely higher in gastric (especially antral) than in intestinal SEMFs and PDGFRA^{Lo} cells.

Transcriptional features of antral and corpus mesenchyme

Having identified substantive differences in sub-epithelial structure and signaling capacity, we examined cell population heterogeneity by mRNA profiling of whole gastric mesenchyme (manually depleted of external smooth muscle) at single-cell (sc) resolution. A total of 34,445 mesenchymal cells (20,624 from corpus and 13,821 from antrum; epithelial contamination was negligible) provided information on at least 2,000 transcripts each (Figure S3A). Consistent with the structures and cells revealed by fluorescence microscopy (Figure 1), graph-based clustering identified substantial fractions of *Pecam1*$^{+}$ endothelial cells, *Acta2*^{hi} *Myh11*^{hi} myocytes, *Acta2*^{lo} *Myh11*^{lo} *Rgs5*$^{+}$ pericytes, and PDGFRA^{+} cells that lack these lineage markers (Figure 3A). Less

than 10% of whole isolates were *Ptprc*$^{+}$ immune cells, smaller than the 45% fraction present in whole SI mesenchyme (McCarthy et al., 2020); only ~1% of cells were glial and <1% showed signs of ongoing cell replication (Figure 3A). Despite structural differences in corpus and antral blood vessels and muscle fibers (Figure 1), the transcriptomes of their constituent cells showed few segmental differences; significant cluster distinctions between stomach regions mapped exclusively to *Pdgfra*$^{+}$ cells (Figures 3B and S3B), justifying our preceding attention on them (Figure 2). Considering both this regional specificity and the substantially broader expression of niche factors compared to other mesenchymal cells (Figure S3C), we focused attention on the 8,671 antral and 6,594 corpus *Pdgfra*$^{+}$ cells.

Graph-based analysis limited to these cells identified 6 clusters: *Pdgfra*^{Hi} and two related but distinct *Pdgfra*^{Lo} cell populations from each gastric segment (Figure 3C). Two *Pdgfra*^{Lo} cell types in the corpus, CorpLo and CorpLo1, were separate on UMAP graphs, but as expected from bulk RNA profiles (Figure 2D), antral *Pdgfra*$^{+}$ cells were less demarcated from each other. Nevertheless, UMAP distinguished *Pdgfra*^{Hi} and *Pdgfra*^{Lo} cells and a large pool (44%) showing intermediate *Pdgfra* and *Cd34* levels (*Pdgfra*^{Int}, Figure 3C) and a distinctive RNA profile (Figure 3D), including EGF-family genes *Ereg* and *Areg*, contractile genes *Acta2* and *Myh11*, the transcription factor (TF) *Sox11*, and prostaglandin synthase *Ptgs2* (Table S2). Transcript levels of *Nrg1*, BMP genes, and *Sfrp1* were similar to those in antral *Pdgfra*^{Hi} cells, while levels of other genes, including extracellular matrix factors *Fbln1* and *Eln*, resembled those in *Pdgfra*^{Lo} cells; some niche factors (e.g., *Nrg1*) express at the same levels as antral but not intestinal *Pdgfra*^{Hi} cells, while others (e.g., *Wnt4*, *Wnt5a*) are discordant (Figures 3E-F and S3D-E). Because flow cytometry separated PDGFRA^{Hi} and PDGFRA^{Lo} cells from *Pdgfra*^{H2BeGFP} mouse corpus better than the antrum (Figure S2A), PDGFRA^{Int} were likely divided between our antral PDGFRA^{Hi} and PDGFRA^{Lo} cell isolates for bulk RNA analysis. Thus, scRNA profiles distinguish mesenchymal populations with possibly divergent functions; we show below that differences in niche activity distinguish *Pdgfra*^{Int} from other antral *Pdgfra*$^{+}$ cells.

Differences between corpus and antral *Pdgfra*^{Lo} subpopulations include expression of known niche factors. Low levels of intestinal niche factors *Grem1* and *Rspo3* apparent in bulk RNA profiles of stomach PDGFRA^{Lo} cells (Figure 2E) are most enriched in the distinct cluster, CorpLo1, and in AntLo (Figure 3G). CorpLo1 also expresses a different spectrum of extracellular matrix genes (high levels of *Has1*, *Dpt* and *Col14a1* – Table S3) compared to CorpLo, suggesting that these populations may localize in different anatomic domains. In general, mRNA levels in gastric *Pdgfra*$^{+}$ cells imply higher BMP tone than in the intestine

because ligand transcripts are expressed significantly not only in SEMFs but also in *Pdgfra*^{Int} and CorpLo, while pathway antagonists express at low levels (Figure S3E). In summary, we identified distinct populations of gastric PDGFRA^{+} cells, at least three from each region, including *Pdgfra*^{Int} in the antrum. We addressed their functions systematically, starting with regionally divergent SEMFs.

Molecular and spatial heterogeneity of antral SEMFs

Gastric *Pdgfra*^{Hi} cells (SEMFs) differ from their intestinal counterparts in high *Fgf7* (antrum) and *Fgf9* (corpus) expression, low levels of the TF gene *Foxl1*, and none of the TF effector of Hedgehog signaling, *Gli1* (Figure 3F and Table S2). Considered separately from other mesenchymal cells, they divided into one homogeneous corpus and two antral subpopulations (Figure 4A). All subpopulations express *Bmp7* and other BMP genes uniformly (Figure S4A), but one antral cluster expresses high *Fgf7* and the EGF ligand *Nrg1*, while the other is marked by high *Bmp3* and *Ctgf* expression and low levels of *Nrg1*, a profile similar to corpus SEMFs (Figure 4A-B). Among these markers, *Fgf7* and *Bmp3* are largely restricted to SEMFs, while the others are enriched in SEMFs but also expressed in other PDGFRA^{+} cells (Figures 3E and S3E). In situ RNA hybridization localized antral *Fgf7*$^{+}$ *Nrg1*$^{+}$ SEMFs to the tops of antral glands, adjacent to foveolae (pits), whereas *Bmp3* and *Ctgf* localize primarily in SEMFs that abut the zone of epithelial cell replication in the lower gland (Figure 4C). As antral SEMF density is higher at gland tops than at the base (Figure S1E), the cell proportions in our scRNA isolates (Figure 4A) further support that these molecularly distinct antral SEMF subpopulations are spatially segregated.

Because *Bmp3* and *Ctgf* are candidate non-canonical BMP antagonists (Bahamonde and Lyons, 2001; Daluiski et al., 2001) and SEMFs expressing those genes lie near proliferative epithelial cells, we asked if they might support antral gland growth *in* vitro. Whereas rNOG readily supported antral organoids *in vitro*, the same concentration of human rBMP3 and of rat or human rCTGF lacked that activity (Figure S4B). No surface marker reliably separated *Bmp3*$^{+}$ *Ctgf*$^{+}$ from *Fgf7*$^{+}$ *Nrg1*$^{+}$ SEMFs, but unfractionated FACS-sorted antral PDGFRA^{Hi} cells (GFP^{Hi} cells from *Pdgfra*^{H2BeGFP} mice) showed no activity in triggering organoid growth from antral glands (Figures 4D and S4C). Corpus PDGFRA^{Hi} cells similarly failed to support corpus glands *in vitro* (Figure S4C); both outcomes differ from the robust stimulation by bulk PDGFRA^{Lo} cells (Figure 1G). Together, these findings reveal spatial and molecular asymmetry of antral SEMFs

without identifying supportive activity for corpus or antral stem-cell compartments, much as intestinal SEMFs lack a discernible support function in organoid assays (McCarthy et al., 2020).

In antral organoids, recombinant human FGF10 induces buds, which are presumed to reflect epithelial maturation (Barker et al., 2010). Because *Fgf7* is abundant in peri-foveolar antral SEMFs, belongs in the same clade as *Fgf10*, and their common receptor, *Fgfr2*, is expressed in antral epithelium (Speer et al., 2012), we considered a function for FGF7 in epithelial differentiation. Indeed, addition of murine rFGF7 to ENRW medium increased antral organoid budding without affecting organoid numbers (Figures 4E and S4D). Constitutive *Fgf7* gene disruption in mice has no reported effects on gastric development or function (Guo et al., 1996) but subtle differentiation defects could have been masked. To assess putative gastric functions in adult mice, we used CRISPR gene editing to flank exon 2 of the *Fgf7* locus with *LoxP* sites (Figure S4E), then introduced the floxed allele onto the $Pdgfra^{Cre(ER\text{-}T2)}$ (Chung et al., 2018) background. $Pdgfra^{Cre(ER\text{-}T2)};Rosa26^{LSL\text{-}tdTomato}$ mouse stomachs revealed robust Cre recombinase activity in $PDGFRA^{Hi}$ and, at lower efficiency, in $PDGFRA^{Lo}$ cells (Figure S4E, see also Figures 1E and S1F). PCR genotyping verified the expected null allele in $Tomato^{+}$ cells isolated from antral $Pdgfra^{Cre(ER\text{-}T2)};Fgf7^{Fl/Fl};Rosa26^{LSL\text{-}TdTomato}$ mesenchyme (Figure S4E). We detected no overt histologic defects or disturbed distribution of antral epithelial proliferative or differentiation markers (Figure S4F) and scRNA profiles of purified wild-type (WT) and $Fgf7^{-/-}$ antral epithelium showed intact proportions and expression characteristics of proliferative and differentiated cells (Figure 4F). Cells from the gland base and proliferative compartments in WT and $Fgf7^{-/-}$ antrum clustered together, and although foveolar cell clusters were not similarly superimposed, foveolar cell transcripts in $Fgf7^{-/-}$ mice differed only subtly from the WT (Table S4). Thus, despite the abundance and specificity of *Fgf7* expression in a spatially discrete subpopulation of antral SEMFs and its effect on organoid budding, the factor's essential and non-redundant role in maintaining the antral epithelium is at most minor and organoid assays reveal no clear stem cell niche role for SEMFs.

A $PDGFRA^{Lo}$ cell population sufficient to support epithelial stem cell growth

Next we examined gastric $Pdgfra^{+}$ cell clusters other than $Pdgfra^{Hi}$ (Figure 3). Considered separately from SEMFs, $Pdgfra^{Lo}$ and $Pdgfra^{Int}$ resolved into 5 objective sub-groups within 3 clusters; the smallest and most distinct cluster corresponds to CorpLo-1 and a tiny fraction of similar antral $Pdgfra^{Lo}$ cells, while the remaining cells cluster by corpus and antral origins (Figures 5A and S5A). Within the large corpus cluster, one sub-group of cells, CorpLo2, shares

expression of a panel of niche factor genes with one antral cell fraction, AntLo, while the other sub-group, CorpLo3, expresses genes (e.g., *Pappa*, *Sox11*, *Postn*, *Nrg1* – Figures 3D and Table S2) that mark *Pdgfra*^{Int} (Figures 5A and S5B). The related populations of antral *Pdgfra*^{Int} and CorpLo3 selectively express BMPs, which inhibit stem cells, and non-canonical Wnts, which lack known niche function (Figures S5B and S5C). Conversely, factors known to constitute the ISC niche, such as *Grem1* and *Rspo3*, are selectively enriched in AntLo, CorpLo2, and the isolated corpus cluster CorpLo1, which uniquely expresses sufficient *Rspo1* to be detected by scRNA-seq (Figures S5B). Thus, scRNA scrutiny separates gastric *Pdgfra*^{Lo} cells into fractions with a capacity to support gastric stem cells (AntLo, CorpLo1, CorpLo2) and those that seem to lack that potential (*Pdgfra*^{Int} and CorpLo3). RNA in situ hybridization in *Pdgfra*^{H2BeGFP} mouse antrum localized *Grem1* and *Ctgf* in adjacent cell layers present beneath antral glands, with limited overlap between cells expressing each marker (Figure 5C). The procedure largely extinguished native GFP^{Lo} cell fluorescence while preserving GFP^{Hi} signals; nevertheless, residual GFP^{Lo} signals were evident in some *Grem1*$^{+}$ and *Ctgf*$^{+}$ cells (Figure 5C). *In situ* hybridization was unreliable in the corpus, likely owing to high tissue mucus. The corresponding scRNA clusters verified that *Ctgf* and *Grem1* expression domains are mutually exclusive in both regions (Figure S5C). The proximity of *Grem1*-expressing mesenchyme to stem cells at the antral gland base is reminiscent of intestinal CD81+ PDGFRA^{Lo} sub-cryptal trophocytes, which help sustain ISCs (McCarthy et al., 2020).

Because unfractionated PDGFRA^{Lo} cells support antral gland growth *in vitro* in the absence of trophic factors (Figure 1G), we sought a molecular marker that might allow isolation of corpus and antral *Grem1*$^{+}$ fractions for functional evaluation. *Cd55*, encoding the tetraspanin CD55, is such a gene, uniquely expressed in AntLo, CorpLo1, and CorpLo2 (Figure 5E), and flow cytometry with CD55 antibody readily separated PDGFRA^{Lo} mesenchymal cells expressing this surface marker from those that do not (Figures 5F and S5E). In co-cultures of gastric glands in basal media supplemented with CD55^{+} or Cd55^{-} fractions of PDGFRA^{Lo} cells isolated by FACS from the respective mesenchyme, only the CD55^{+} fraction demonstrated supportive activity (Figures 5G and S5F-G). Neither fraction induced spheroid formation from SI crypts, but SI trophocytes induced spheroid growth from isolated corpus and antral glands (Figure 5H). Together, these findings reveal a population of gastric PDGFRA^{Lo} CD55^{+} cells that express the BMPi *Grem1* and Wnt potentiating RSPOs and is selectively trophic toward gastric epithelium.

DISCUSSION

To ensure a proper epithelial cell census, the stem cell niches that surround specific spaces within intestinal crypts and gastric glands generate Wnt, BMP, and other signaling gradients that favor cell replication and hinder differentiation (Farin et al., 2012; Haramis et al., 2004; Kabiri et al., 2014; Sigal et al., 2017; Sigal et al., 2019). PDGFRA^{+} cells generate the requisite BMP gradient around intestinal crypts (McCarthy et al., 2020) but signaling sources and their arrangements are not known in the gastric corpus and antrum, where gland structure is markedly different (Kim et al., 2020). As a group, PDGFRA^{+} cells constitute the most diverse mesenchymal population and our combination of bulk and single-cell RNA studies, high-resolution microscopy, and organoid co-cultures identified anatomically, molecularly, and functionally distinct subpopulations. While in the corpus the analysis highlighted the presence of three spatially separated clusters of *Pdgfra*-expressing cells, one being PDGFRA^{Hi} and the other two being PDGFRA^{Lo}, antral cells appeared to be more closely related in the UMAP plot. In fact, on top of the canonical PDGFRA^{Hi} and PDGFRA^{Lo} groups, we identified an antrum-specific population of intermediate *Pdgfra*-expressing cells that are largely absent from the corpus or the SI, remarking the differences between gastrointestinal regions. Moreover, analysis of BMP ligands and BMP inhibitors gene expression, indicated diffuse higher levels of BMP signaling in the gastric environment compared with the SI one, highlighting commonalities and regional differences in niche support along the digestive tract.

ISMFs in the SI present a fairly homogeneous transcriptional asset, with high expression levels of BMP ligands and low levels of BMPi and Wnt signaling genes. Similarly, corpus presents a uniform population of PDGFRA^{Hi}. On the contrary, in the antrum we found the presence of two distinct sub-populations, different in their gene expression pattern and spatial distribution. *Fgf7*$^{+}$;*Nrg1*$^{+}$ PDGFRA^{Hi} cells specifically situate near the pit of the glands, where differentiated foveolar cells resides, while *Bmp3*$^{+}$ cells position in the lower half of the gland, in the epithelial cells proliferation zone. Unfortunately, separate these two populations was technically challenging, and we were not able to assess their activity on stem cells *in vitro* separately. FGF7 belongs to the same family as FGF10, a factor used to induce stem cell maturation *in vitro* (Barker et al., 2010). Considering the high expression of mesenchymal *Fgf7* near the foveolar cells, a distinctive trait of antral ISMFs, and the activity of recombinant FGF7 on organoids, we opted for its ablation *in vivo* in PDGFRA^{+} cells to study the effect of its deficiency. Despite the abundance of its transcript, *Fgf7* gene ablation had no effect on epithelium differentiation and gene expression patterns in homeostatic conditions. Further analysis would be needed to

address the role it may play in disease, challenging the system with *stimuli* such as *Helicobacter pylori* infection or cancer development.

Similarly to what observed in the SI, the analysis of gastric PDGFRA^{Lo} cells showed the presence of two distinct sub-populations in both gastric regions: a trophic population, sufficient for gastric organoids growth in vitro, and a non-trophic one, unable to prompt organoids formation. These two populations were marked by differential expression of *Cd55* gene, as opposed to *Cd81* in the SI. Gastric CD55^{+} trophocytes presented high expression of Wnt signaling enhancer *Rspo3*, BMP inhibitor *Grem1* and putative BMP inhibitor *Ctgf*. Moreover, they showed low to no expression of BMP ligands, such as *Bmp2*, *5* and *7*. Despite the similarities to the small intestinal trophocytes, gastric CD55+ cells were unable to sustain organoids formation from SI crypts in absence of growth factors. In fact, they lack expression of factors such as *Rspo3* and present significant lower levels of *Grem1*, suggesting that BMP inhibition is much more necessary for SI stem cells activity than for the gastric ones. RNA *in situ* hybridization localized *Grem1*$^{+}$ and *Ctgf*$^{+}$ CD55^{+} PDGFRA^{Lo} below the gland bottom in the antrum, corresponding with the stem cell zone and concordant with their trophic function. Technical issues prevented us from uncover the localization of CD55^{+} cells in the corpus, however we expect them to be located at the isthmus level, where the epithelial stem cells and transit amplifying cells reside.

Our study finely depicts the spatial and functional structure of the gastric mesenchyme, highlighting remarkable regional differences between gastrointestinal compartments. High-resolution imaging data, supported by transcriptomic analysis at single cell level of the corpus and the antrum, establish a roadmap for further studies on the role of mesenchymal populations in homeostasis and disease.

Author Contributions

E.M., N.M. and R.A.S. conceived and designed the study; E.M., G.T., N.M. and A.M. performed experiments; E.M., S.M. and R.H. performed computational analyses; D.S., K.Z., Y.F. and S.H.O. generated the *Fgf7*$^{fl/fl}$ mouse model; K.H. assisted with image signal quantitation; E.M. and R.A.S. analyzed and interpreted data and wrote the manuscript, with input and approval from all authors.

Acknowledgments

Supported by NIH grant R01DK121540, the Intestinal Stem Cell Consortium of NIDDK and NIAID (U01DK103152), and a gift from the Sarah Rhodes Fund. We gratefully acknowledge the contributions of imaging, flow cytometry, and organoid core facilities at the Harvard Digestive Diseases Center (P30DK034854) and the Dana-Farber Cancer Institute.

METHODS

Mouse models and treatment

All animal procedures were approved by Animal Care and Use Committees at Dana-Farber Cancer Institute. Mice were housed in a pathogen-free animal facility and maintained on a 12-h light/dark cycle at constant temperature and humidity, with *ad libitum* access to food and water. Strains were maintained on a mixed *C57BL/6* background. Male and females aged 8-16 weeks were used. Genotypes were identified by PCR analysis of genomic DNA isolated from mouse toes. *Pdgfra*^{H2BeGFP} mice were purchased from Jackson Laboratories (JAX strain 007669), as well as *Pdgfra-CreER*^{T2} (JAX strain 032770), *Rosa26*$^{Lsl\text{-}TdTomato}$ (JAX strain 007908) and *Rosa26*$^{mT/mG}$ strain (JAX strain 07676). *Rosa26*$^{mT/mG}$ mice were crossed with *Pdgfra-CreER*^{T2} to generate *Pdgfra-CreER*^{T2}*;Rosa26*$^{mT/mG}$. Cre-recombinase activity was induced by 2 mg/day tamoxifen (Sigma Aldrich T5648) i.p. injection for 4 consecutive days, and mice were used to visualize *Pdgfra*-expressing cells. *Fgf7*$^{fl/fl}$ mice were generated in collaboration with D. Seruggia and S.H. Orkin laboratories, and crossed with *Pdgfra-CreER*^{T2} and *Rosa26*$^{Lsl\text{-}TdTomato}$ to obtain *Pdgfra-CreER*^{T2}*;Fgf7*$^{fl/fl}$*;Rosa26*$^{LSL\text{-}TdTomato}$ mice. 2mg/day of tamoxifen (Sigma Aldrich T5648) were injected i.p. to induce cell specific Cre recombinase activation and genetic recombination. *Cre*-negative littermates were used as controls.

Fgf7 conditional mouse generation

Conditional knockout of *Fgf7* was obtained by genome editing in 1-cell embryos. Adeno-associated virus (AAVs) and electroporation were used to deliver a targeting vector along with Cas9 protein and two sgRNA, as previously described (Mehta et al., 2022). The targeting vector consisted in the sequence of *Fgf7* exon 2, flanked by LoxP sites and surrounded by short homology arms. To prevent re-cutting after homologous recombination, single-nucleotide substitutions at the PAM motifs were included in the targeting vector. Oligonucleotides used for *in vitro* transcription of sgRNAs and for genotyping are included in Table S5.

Gastrointestinal organoids culture

Organoids were generated from wild type murine intestinal crypts or gastric glands. Briefly, after dissection, intestinal crypts were isolated from the first half of the intestine incubating the tissue at 4 degrees in cold 2 mM EDTA-PBS as previously described (Sato et al., 2009). Intestinal crypts were plated in Matrigel (Corning 356234) and cultured in complete media (DMEM/F12 supplemented with Glutamax, HEPES, Penicillin, Streptomycin, Neomycin, Primomycin, N2, B27, 1mM N-Acetylcysteine, 50 µg/mL murine rEGF, 100 µg/mL murine rNoggin, 10% Rspo1 conditioned media). Gastric glands were isolated from antrum or corpus separately, incubating the tissue in 10 mM EDTA-PBS at room temperature as previously described (Mahe et al., 2013; Singh et al., 2022). Glands were separated from the stroma and muscularis mucosa by gentle scraping, washed in PBS and cultured in complete media (same as small intestinal organoid complete media with the addition of 10% Afamin/Wnt3a conditioned media, MBL International Corporation, J2-001) or as specified in the text.

Organoids gene expression quantification

Organoids from antrum and corpus were growth in complete media for 4 days. Droplets were washed with cold PBS, gently detached from the plate and incubated 20 minutes in Cell Recovery solution (Corning, 354270) to depolymerized Matrigel. Organoids were then collected by centrifugation and resuspended in Trizol Reagent (Thermo Fisher Scientific). Total RNA was isolated with RNeasy Mini Kit (QIAGEN). 1µg of total RNA was reverse transcribed using SuperScript III First-Strand Synthesis System for RT-PCR (Invitrogen, 18080-051). Gene expression levels were measured using Power SYBR Green (Life Technologies, 4367659) on a LightCycler 480 instrument (Roche). Sequence of forward and reverse primers are provided in Table S6. Gene expression levels were normalized to *Gapdh* expression ($2^{-\Delta Ct}$).

Mesenchymal cells isolation

Intestinal, antral and corpus mesenchyme was isolated similarly to previous reports (Kurahashi et al., 2013; McCarthy et al., 2020; Stzepourginski et al., 2015). Tissue was collected after perfusing adult *Pdgfra*^{H2BeGFP} with cold PBS. After manual muscle removal, epithelium was removed by shaking the tissue in pre-warmed chelation buffer (10 mM EDTA, 5% FBS, 1 mM Dithiothreitol-DTT, HEPES in HBSS buffer) for 20 minutes at 37°C, 250rpm. The tissue was then washed with PBS and digested for 10 minutes at 37°C in 3 mg/ml collagenase II (Worthington, LS004176) in HBSS complemented with 5% FBS and HEPES. Cells were harvested by centrifugation at 300g for 5 minutes. For bulk RNA sequencing, cells were sorted

on a BD FACSAria II cell sorter, gating on DAPI negative cells to identify live cells, and GFP high and GFP low to sort *Pdgfra* high or low expressing cells. For single cell-RNA sequencing all DAPI negative cells were sorted.

Organoid/mesenchymal cells co-culture

For co-culture experiments the whole mesenchyme fraction was isolated and plated on tissue culture plates in DMEM/F12 medium supplemented with 10% FBS, penicillin, streptomycin, neomycin, primomycin, Glutamax, HEPES. Two days after isolation cells were washed with PBS and removed from the plate with 0.25% Trypsin (5 minutes at 37°C), washed and stained with the corresponding antibodies: SI mesenchyme with biotin-CD81 primary antibody (13 0811 81, eBioscience), followed by incubation with streptavidin-APC conjugate secondary antibody (17 4317 82, eBioscience); A or C cells were incubated with CD55 conjugated antibody (131803, BioLegend). 5,000 cells were co-cultured with ~20 glands or crypts in 5 µl Matrigel droplets in basal media with no recombinant factors (DMEM/F12 supplemented with Glutamax, HEPES, Penicillin, Streptomycin, Neomycin, Primomycin, N2, B27, 1mM N-Acetylcysteine).

Immunohistochemistry and imaging

Routine immunohistochemistry was performed on fixed tissue placed in OCT compound (Tissue-Tek, VWR Scientific, 4583). 10 µm sections were prepared using a Leica cryostat.

Whole-mount tissue immunohistochemistry was performed as described (Bernier-Latmani and Petrova, 2016). Mice were perfused with ice cold PBS, followed by 4% PFA. Antrum and corpus were analyzed separately and pinned onto agarose plates. Tissues were treated with mucolytic solution (20mM N-Acetyl Cysteine, 20mM DTT, in PBS) for 15 minutes at room temperature, followed by 15 minutes incubation in 4% PFA. Muscle layers were manually removed before overnight fixation with 15% picric acid, 0.5% PFA in PBS. On day 2, tissue was washed in PBS and placed in 10% sucrose for 4 hours, then 20% sucrose overnight. On day 3, tissue was placed in blocking buffer (0.5% BSA, 0.6% Triton X-100, 0.05% normal goat serum and 0.0005% sodium azide) for 6 hours, followed by overnight incubation with primary antibodies. On day 4, after 5 hourly washes in wash buffer (0.3% Triton X-100 in PBS), tissue was incubated with conjugated-secondary antibodies and DAPI. The next day tissue was washed for 5 hours, changing wash buffer every 30 minutes, and fixed in 4% PFA. Hand-cut 1 mm fragments of tissue were positioned on glass slides with imaging spacers (Grace Bio-Labs SecureSeal, Sigma Aldrich), cleared for 30 minutes with FocusClear (CelExplorer, FC-101) and mounted with VectaShield (Thermo Fisher Scientific) mounting media. Tissues from three

independent mice were imaged using either a Leica SP5X laser scanning confocal microscope (Leica Microsystems CMS GmbH) or a Zeiss LSM980 microscope and ZEN Desk 3.4 software (Carl Zeiss GmbH). Picture were analyzed using Fiji (Schindelin et al., 2012). Video were made with ZEN Desk 3.4 software. The following primary antibodies were used at 1:500 dilution unless otherwise specified: CD31 (BD Cell Analysis, 557355); Laminin (Sigma Aldrich, L9393); alpha-smooth muscle actin1 (Abcam, ab5694); PDGFRA (1:100; R&D Systems, AF1062); MUC5AC (Cell Signaling Technology, 6119S); Gastrin (Abcam, ab232775); Somatostatin (Santa Cruz Biotechnology, sc-55565); secondary antibodies (Alexa Fluor, Invitrogen). DAPI 1:1000 dilution was used to detect cellular nuclei.

RNAscope in situ hybridization

mRNA detection for spatial localization of cell sub-populations was carried out by RNAscope method (RNAscope Multiplex Fluorescent Reagent Kit v2, ACD) (McCarthy et al., 2020; Wang et al., 2012a). Probes designed by Advanced Cell Diagnostic were used to detect *Grem1* (314741), Ctgf (314541), *Fgf7* (443521), *Bmp3* (428461), *Nrg1* (468841) transcripts following manufacturer's recommendation after 5 minutes of target retrieval. GFP signal was revealed by immunohistochemistry using GFP antibody (1:100 Abcam, ab6556) as previously described (McCarthy et al., 2020). Tissues were imaged using Leica SP5X laser scanning confocal microscope (Leica Microsystems CMS GmbH). Fluorescent signal distribution along glands was quantified with Fiji.

Bulk RNA sequencing

Pdgfra-expressing cells were isolated and FACS-sorted from antrum and corpus as described above and placed in Trizol Reagent (Thermo Fisher Scientific). Total RNA was isolated with RNeasy Micro Kit (QIAGEN) and used for library preparation (5-10 ng) using SMART-Seq v4 Ultra Low Input RNA Kit (Clontech). Libraries were sequenced on Novaseq platform (Illumina).

Single cell RNA sequencing

Whole mesenchyme was isolated from antrum and corpus as described above, with elimination of dead cells by DAPI FACS-sorting. About 10,000 cells were loaded onto a 10X Genomics Chip G. Libraries were prepared according to manufacturer's protocol using 10X Single-Cell 3' v3.1 chemistry (10X Genomics PN-1000128) and sequenced on the NovaSeq platform (Illumina).

Data processing and analysis:

Image segmentation and quantification

Organoid images were segmented using Cellpose plugin in CellProfiler (Stirling et al., 2021; Stringer et al., 2021). 4 to 12 images were taken into consideration per treatment. Segmentation masks were generated using Cellpose pre-trained model “cyto” and a cell diameter of 150 pixels (minimum size of 15 pixels and flow threshold 0.7). The segmented masks and original images were then fed into CellProfiler to quantify organoid numbers and area occupied for each organoid.

GFP positive cells were quantified with Cellpose and Cellprofiler. 6 images per gastric region were used for the quantification, representative ones are reported. The masks were generated using Cellpose pre-trained model “cyto2” and a cell diameter of 43 pixels. Each image contains about 300 segmented GFP-positive cells and more than 99% of the cells were include in the segmentation. The segmented masks and original images were then fed into CellProfiler to study GFP^+ cell distribution.

Bulk RNA-sequencing

Data were aligned to mouse reference genome mm10 using the Viper pipeline with default settings (Cornwell et al., 2018). Data quality was verified using RSeQC (Wang et al., 2012b). R platform 4.2.1 was used for further analyses. Reads of genes belonging to gastric epithelial signature and to sex-chromosomes were excluded from the analysis. Data normalization and differential gene expression analysis ($p_{adj} < 0.05$; $|\log_2 FoldChange| > 1.5$) were performed with DESeq2 package (Love et al., 2014). Reads per kilobase per million (RPKM) values were generated from normalized counts. Pearson correlation coefficients were calculated from DESeq2 normalized counts and plotted using Corrplot package (Wei et al., 2017). Principal component analysis (PCA) was done using Rlog-transformed counts, as well as the expression heatmap of selected factors. The Integrative Genome Viewer Tracks (IGV tracks) were generated from RPKM-normalized bigwigs loaded into IGV 2.15.4 (Broad Institute). Data from small intestine data were previously published (GSE130681) (McCarthy et al., 2020).

Single cell RNA sequencing

Samples were aligned to the mm10 genome using 10x Genomics Cell Ranger 3.0.2 with default parameters (Zheng et al., 2017). Bioinformatic analyses were conducted via R version 4.2.1 Single-cell analyses used Seurat 4.1.0 (Hao et al., 2021). Cells were filtered for a minimum of 1,000 and <12% mitochondrial reads. Data were merged and normalized using sctransform

(Hafemeister and Satija, 2019). Cell features were detected with the FindVariableFeatures function (2,000 features, selection method “vst”). The first 15 principal components were taken to run uniform manifold approximation and projection (UMAP) algorithms (McInnes et al., 2018). Cell types were identified using established marker genes detected by the “FindAllMarkers” function in Seurat2 (min.pct=0.25, test “roc”).

MetaNeighbor-AUROC analysis is a robust tool to assess similarities between two cell types and it was performed to compare gastric mesenchymal populations. In brief, highly variable genes in the dataset were identified and used to train an algorithm to predict the cell type of a given cell by the expression of their nearest neighbors. To calculate the ’similarity’ between cell types A and B across two samples, the cell type annotation from one group was hidden and a score was used to represents how often a cell in cell type A is predicted to belong to cell type B versus all other cell types (AUROC score). A higher score indicates more similarity between two cell types.

Quantification and statistical analysis

Prism9 (GraphPad Inc) was used for statistical analysis of all data. Specific tests and significance levels are indicated in figure legends.

Graphical illustrations were created with BioRender.com

REFERENCES

Abreu, J.G., Ketpura, N.I., Reversade, B., and De Robertis, E.M. (2002). Connective-tissue growth factor (CTGF) modulates cell signalling by BMP and TGF-beta. Nat Cell Biol *4*, 599-604.
Aoki, R., Shoshkes-Carmel, M., Gao, N., Shin, S., May, C.L., Golson, M.L., Zahm, A.M., Ray, M., Wiser, C.L., Wright, C.V.*, et al.* (2016). Foxl1-expressing mesenchymal cells constitute the intestinal stem cell niche. Cell Mol Gastroenterol Hepatol *2*, 175-188.
Bahamonde, M.E., and Lyons, K.M. (2001). BMP3: to be or not to be a BMP. J Bone Joint Surg Am *83-A Suppl 1*, S56-62.
Barker, N., Huch, M., Kujala, P., van de Wetering, M., Snippert, H.J., van Es, J.H., Sato, T., Stange, D.E., Begthel, H., van den Born, M.*, et al.* (2010). Lgr5(+ve) stem cells drive self-renewal in the stomach and build long-lived gastric units in vitro. Cell Stem Cell *6*, 25-36.
Bernier-Latmani, J., and Petrova, T.V. (2016). High-resolution 3D analysis of mouse small-intestinal stroma. Nat Protoc *11*, 1617-1629.
Chung, M.I., Bujnis, M., Barkauskas, C.E., Kobayashi, Y., and Hogan, B.L.M. (2018). Niche-mediated BMP/SMAD signaling regulates lung alveolar stem cell proliferation and differentiation. Development *145*.
Cornwell, M., Vangala, M., Taing, L., Herbert, Z., Koster, J., Li, B., Sun, H., Li, T., Zhang, J., Qiu, X.*, et al.* (2018). VIPER: Visualization Pipeline for RNA-seq, a Snakemake workflow for efficient and complete RNA-seq analysis. BMC Bioinformatics *19*, 135.
Daluiski, A., Engstrand, T., Bahamonde, M.E., Gamer, L.W., Agius, E., Stevenson, S.L., Cox, K., Rosen, V., and Lyons, K.M. (2001). Bone morphogenetic protein-3 is a negative regulator of bone density. Nat Genet *27*, 84-88.
Degirmenci, B., Valenta, T., Dimitrieva, S., Hausmann, G., and Basler, K. (2018). GLI1-expressing mesenchymal cells form the essential Wnt-secreting niche for colon stem cells. Nature *558*, 449-453.
Farin, H.F., Van Es, J.H., and Clevers, H. (2012). Redundant sources of Wnt regulate intestinal stem cells and promote formation of Paneth cells. Gastroenterology *143*, 1518-1529 e1517.
Greicius, G., Kabiri, Z., Sigmundsson, K., Liang, C., Bunte, R., Singh, M.K., and Virshup, D.M. (2018). PDGFRalpha(+) pericryptal stromal cells are the critical source of Wnts and RSPO3 for murine intestinal stem cells in vivo. Proc Natl Acad Sci U S A *115*, E3173-E3181.
Guo, L., Degenstein, L., and Fuchs, E. (1996). Keratinocyte growth factor is required for hair development but not for wound healing. Genes Dev *10*, 165-175.
Hafemeister, C., and Satija, R. (2019). Normalization and variance stabilization of single-cell RNA-seq data using regularized negative binomial regression. Genome Biol *20*, 296.
Hamilton, T.G., Klinghoffer, R.A., Corrin, P.D., and Soriano, P. (2003). Evolutionary divergence of platelet-derived growth factor alpha receptor signaling mechanisms. Mol Cell Biol *23*, 4013-4025.
Hao, Y., Hao, S., Andersen-Nissen, E., Mauck, W.M., 3rd, Zheng, S., Butler, A., Lee, M.J., Wilk, A.J., Darby, C., Zager, M.*, et al.* (2021). Integrated analysis of multimodal single-cell data. Cell *184*, 3573-3587 e3529.
Haramis, A.P., Begthel, H., van den Born, M., van Es, J., Jonkheer, S., Offerhaus, G.J., and Clevers, H. (2004). De novo crypt formation and juvenile polyposis on BMP inhibition in mouse intestine. Science *303*, 1684-1686.
Jarde, T., Chan, W.H., Rossello, F.J., Kaur Kahlon, T., Theocharous, M., Kurian Arackal, T., Flores, T., Giraud, M., Richards, E., Chan, E.*, et al.* (2020). Mesenchymal Niche-Derived Neuregulin-1 Drives Intestinal Stem Cell Proliferation and Regeneration of Damaged Epithelium. Cell Stem Cell *27*, 646-662 e647.
Kabiri, Z., Greicius, G., Madan, B., Biechele, S., Zhong, Z., Zaribafzadeh, H., Edison, Aliyev, J., Wu, Y., Bunte, R.*, et al.* (2014). Stroma provides an intestinal stem cell niche in the absence of epithelial Wnts. Development *141*, 2206-2215.

Kapalczynska, M., Lin, M., Maertzdorf, J., Heuberger, J., Muellerke, S., Zuo, X., Vidal, R., Shureiqi, I., Fischer, A.S., Sauer, S.*, et al.* (2022). BMP feed-forward loop promotes terminal differentiation in gastric glands and is interrupted by H. pylori-driven inflammation. Nat Commun *13*, 1577.
Karam, S.M. (1993). Dynamics of epithelial cells in the corpus of the mouse stomach. IV. Bidirectional migration of parietal cells ending in their gradual degeneration and loss. Anat Rec *236*, 314-332.
Karam, S.M., and Leblond, C.P. (1993a). Dynamics of epithelial cells in the corpus of the mouse stomach. I. Identification of proliferative cell types and pinpointing of the stem cell. Anat Rec *236*, 259-279.
Karam, S.M., and Leblond, C.P. (1993b). Dynamics of epithelial cells in the corpus of the mouse stomach. II. Outward migration of pit cells. Anat Rec *236*, 280-296.
Karam, S.M., and Leblond, C.P. (1993c). Dynamics of epithelial cells in the corpus of the mouse stomach. III. Inward migration of neck cells followed by progressive transformation into zymogenic cells. Anat Rec *236*, 297-313.
Kim, J.E., Fei, L., Yin, W.C., Coquenlorge, S., Rao-Bhatia, A., Zhang, X., Shi, S.S.W., Lee, J.H., Hahn, N.A., Rizvi, W.*, et al.* (2020). Single cell and genetic analyses reveal conserved populations and signaling mechanisms of gastrointestinal stromal niches. Nat Commun *11*, 334.
Kurahashi, M., Nakano, Y., Peri, L.E., Townsend, J.B., Ward, S.M., and Sanders, K.M. (2013). A novel population of subepithelial platelet-derived growth factor receptor alpha-positive cells in the mouse and human colon. Am J Physiol Gastrointest Liver Physiol *304*, G823-834.
Leushacke, M., Ng, A., Galle, J., Loeffler, M., and Barker, N. (2013). Lgr5(+) gastric stem cells divide symmetrically to effect epithelial homeostasis in the pylorus. Cell Rep *5*, 349-356.
Love, M.I., Huber, W., and Anders, S. (2014). Moderated estimation of fold change and dispersion for RNA-seq data with DESeq2. Genome Biol *15*, 550.
Mahe, M.M., Aihara, E., Schumacher, M.A., Zavros, Y., Montrose, M.H., Helmrath, M.A., Sato, T., and Shroyer, N.F. (2013). Establishment of Gastrointestinal Epithelial Organoids. Curr Protoc Mouse Biol *3*, 217-240.
Matsuo, J., Kimura, S., Yamamura, A., Koh, C.P., Hossain, M.Z., Heng, D.L., Kohu, K., Voon, D.C., Hiai, H., Unno, M.*, et al.* (2017). Identification of Stem Cells in the Epithelium of the Stomach Corpus and Antrum of Mice. Gastroenterology *152*, 218-231 e214.
McCarthy, N., Manieri, E., Storm, E.E., Saadatpour, A., Luoma, A.M., Kapoor, V.N., Madha, S., Gaynor, L.T., Cox, C., Keerthivasan, S.*, et al.* (2020). Distinct Mesenchymal Cell Populations Generate the Essential Intestinal BMP Signaling Gradient. Cell Stem Cell *26*, 391-402 e395.
McInnes et al., (2018). UMAP: Uniform Manifold Approximation and Projection. Journal of Open Source Software, 3(29), 861, https://doi.org/10.21105/joss.00861
Mehta, S., Buyanbat, A., Kai, Y., Karayel, O., Goldman, S.R., Seruggia, D., Zhang, K., Fujiwara, Y., Donovan, K.A., Zhu, Q.*, et al.* (2022). Temporal resolution of gene derepression and proteome changes upon PROTAC-mediated degradation of BCL11A protein in erythroid cells. Cell Chem Biol *29*, 1273-1287 e1278.
Murakami, K., Terakado, Y., Saito, K., Jomen, Y., Takeda, H., Oshima, M., and Barker, N. (2021). A genome-scale CRISPR screen reveals factors regulating Wnt-dependent renewal of mouse gastric epithelial cells. Proc Natl Acad Sci U S A *118*.
Muzumdar, M.D., Tasic, B., Miyamichi, K., Li, L., and Luo, L. (2007). A global double-fluorescent Cre reporter mouse. Genesis *45*, 593-605.
Nguyen, T.Q., Roestenberg, P., van Nieuwenhoven, F.A., Bovenschen, N., Li, Z., Xu, L., Oliver, N., Aten, J., Joles, J.A., Vial, C.*, et al.* (2008). CTGF inhibits BMP-7 signaling in diabetic nephropathy. J Am Soc Nephrol *19*, 2098-2107.
Sato, T., Vries, R.G., Snippert, H.J., van de Wetering, M., Barker, N., Stange, D.E., van Es, J.H., Abo, A., Kujala, P., Peters, P.J.*, et al.* (2009). Single Lgr5 stem cells build crypt-villus structures in vitro without a mesenchymal niche. Nature *459*, 262-265.

Schindelin, J., Arganda-Carreras, I., Frise, E., Kaynig, V., Longair, M., Pietzsch, T., Preibisch, S., Rueden, C., Saalfeld, S., Schmid, B.*, et al.* (2012). Fiji: an open-source platform for biological-image analysis. Nat Methods *9*, 676-682.
Shinohara, M., Mao, M., Keeley, T.M., El-Zaatari, M., Lee, H.J., Eaton, K.A., Samuelson, L.C., Merchant, J.L., Goldenring, J.R., and Todisco, A. (2010). Bone morphogenetic protein signaling regulates gastric epithelial cell development and proliferation in mice. Gastroenterology *139*, 2050-2060 e2052.
Shoshkes-Carmel, M., Wang, Y.J., Wangensteen, K.J., Toth, B., Kondo, A., Massasa, E.E., Itzkovitz, S., and Kaestner, K.H. (2018). Subepithelial telocytes are an important source of Wnts that supports intestinal crypts. Nature *557*, 242-246.
Sigal, M., Logan, C.Y., Kapalczynska, M., Mollenkopf, H.J., Berger, H., Wiedenmann, B., Nusse, R., Amieva, M.R., and Meyer, T.F. (2017). Stromal R-spondin orchestrates gastric epithelial stem cells and gland homeostasis. Nature *548*, 451-455.
Sigal, M., Reines, M.D.M., Mullerke, S., Fischer, C., Kapalczynska, M., Berger, H., Bakker, E.R.M., Mollenkopf, H.J., Rothenberg, M.E., Wiedenmann, B.*, et al.* (2019). R-spondin-3 induces secretory, antimicrobial Lgr5(+) cells in the stomach. Nat Cell Biol *21*, 812-823.
Singh, H., Seruggia, D., Madha, S., Saxena, M., Nagaraja, A.K., Wu, Z., Zhou, J., Huebner, A.J., Maglieri, A., Wezenbeek, J.*, et al.* (2022). Transcription factor-mediated intestinal metaplasia and the role of a shadow enhancer. Genes Dev *36*, 38-52.
Speer, A.L., Al Alam, D., Sala, F.G., Ford, H.R., Bellusci, S., and Grikscheit, T.C. (2012). Fibroblast growth factor 10-fibroblast growth factor receptor 2b mediated signaling is not required for adult glandular stomach homeostasis. PLoS One *7*, e49127.
Stirling, D.R., Swain-Bowden, M.J., Lucas, A.M., Carpenter, A.E., Cimini, B.A., and Goodman, A. (2021). CellProfiler 4: improvements in speed, utility and usability. BMC Bioinformatics *22*, 433.
Stringer, C., Wang, T., Michaelos, M., and Pachitariu, M. (2021). Cellpose: a generalist algorithm for cellular segmentation. Nat Methods *18*, 100-106.
Stzepourginski, I., Eberl, G., and Peduto, L. (2015). An optimized protocol for isolating lymphoid stromal cells from the intestinal lamina propria. J Immunol Methods *421*, 14-19.
Todisco, A. (2017). Regulation of Gastric Metaplasia, Dysplasia, and Neoplasia by Bone Morphogenetic Protein Signaling. Cell Mol Gastroenterol Hepatol *3*, 339-347.
Wang, F., Flanagan, J., Su, N., Wang, L.C., Bui, S., Nielson, A., Wu, X., Vo, H.T., Ma, X.J., and Luo, Y. (2012a). RNAscope: a novel in situ RNA analysis platform for formalin-fixed, paraffin-embedded tissues. J Mol Diagn *14*, 22-29.
Wang, L., Wang, S., and Li, W. (2012b). RSeQC: quality control of RNA-seq experiments. Bioinformatics *28*, 2184-2185.
Wei T, Simko V, Levy M, Xie Y, Jin Y, and Zemla J. (2017). *R package "corrplot": Visualization of a correlation matrix* (version 0.84). https://github.com/taiyun/corrplot.
Wolffling, S., Daddi, A.A., Imai-Matsushima, A., Fritsche, K., Goosmann, C., Traulsen, J., Lisle, R., Schmid, M., Reines-Benassar, M.D.M., Pfannkuch, L.*, et al.* (2021). EGF and BMPs Govern Differentiation and Patterning in Human Gastric Glands. Gastroenterology *161*, 623-636 e616.
Ye, W., Takabayashi, H., Yang, Y., Mao, M., Hibdon, E.S., Samuelson, L.C., Eaton, K.A., and Todisco, A. (2018). Regulation of Gastric Lgr5+ve Cell Homeostasis by Bone Morphogenetic Protein (BMP) Signaling and Inflammatory Stimuli. Cell Mol Gastroenterol Hepatol *5*, 523-538.
Zheng, G.X., Terry, J.M., Belgrader, P., Ryvkin, P., Bent, Z.W., Wilson, R., Ziraldo, S.B., Wheeler, T.D., McDermott, G.P., Zhu, J.*, et al.* (2017). Massively parallel digital transcriptional profiling of single cells. Nat Commun *8*, 14049.

MAIN FIGURES

Figure 1

A) Schematic representation of gastrointestinal regions and glandular stomach epithelium organization. Corpus and antrum are composed of different cell types which reflect their function.

B) Antrum (top) and corpus (bottom) glands cross-sections, showing muscle fibers, marked with α-smooth muscle actin (SMA1, yellow) and capillaries, marked with CD31 (red). Scale bar 50um.

C) Whole-mount 3D rendering of corpus (left) and antrum (right) glands highlighting muscle fibers (SMA1, yellow) and capillaries (CD31, red) organization. Scale bar 50um

D) Whole-mount 3D rendering of corpus (left) and antrum (top right) glands in *Pdgfra*^{H2BeGFP} mice. Laminin (yellow) marks the basal lamina and emphasizes gland pits. Gland cross-sections are represented in 1 and 2, corresponding to the dashed lines in the 3D rendering pictures. PDGFRA^{Hi} cells are in neon green while PDGFRA^{Lo} cells are in light green. Immunostaining with PDGFRA antibody shows the extended net of *Pdgfra*$^{+}$ cell cytoplasm. Scale bar 50um.

E) Extracted frames from video 1 (left, corpus) and 2 (right, antrum) showing *Pdgfra*$^{+}$ cells (green) in *PdgfraCre*$^{ERT2+}$*;Rosa26*$^{mT/mG}$ mouse. DAPI in blue. *Pdgfra*$^{+}$ cells cover the basal side of the epithelium with their extensions.

F) Schematic representation of *Pdgfra*-expressing cells distribution in relation to epithelial cells. PDGFRA^{Hi} cells in dark green and PDGFRA^{Lo} cells in light green.

G) Co-culture of intestinal crypts with PDGFRA^{Lo} cells isolated from small intestine (SI), corpus (C) or antrum (A) in Matrigel. PDGFRA^{Lo} cells from antrum or corpus are not able to induce SI organoid formation in absence of rNOGGIN and RSPO1.

Figure 2

A) Quantification of gastric organoid growth in different media conditions. Dots indicate factor concentration: full, half or no factor (empty dot). Factors: E: recombinant EGF; N: recombinant NOGGIN; R: RSPO1 conditioned media; W: AFAMIN/WNT3A conditioned media. Bars represent mean ± SEM values (n = 4-8). Significance of differences was determined by one-way ANOVA comparing each condition with control organoids growth in full concentration of all factors (ENRW). *$p<0.05$; **$p<0.01$; ***$p < 0.001$; ****$p<0.0001$.

B) Pearson correlations among duplicated RNA-seq libraries prepared from PDGFRA^{+} cells isolated from different regions of the gastrointestinal tract. PDGFRA^{+} cells from the stomach are substantially different from the intestinal ones. SI, small intestine; A, antrum; C, corpus

C) Volcano plots representing differentially expressed genes ($q < 0.05$; $\log_2$ fold-difference >1.5) between antrum and small intestine (SI) (top) or corpus and antrum (bottom) PDGFRA^{Hi} cells. Selected genes are shown. Venn diagrams represent the number of differentially expressed gene.

D) Heatmap representing population signature genes ($q < 0.05$; $\log_2$ fold-difference >1.5; k-means = 6). D') Integrative genome viewer (IGV) tracks showing RNA-seq data for genes highly expressed in SI PDGFRA^{Lo} cells. *Actb* controls for proper normalization of read counts and the numbers in parentheses refer to the range of signal values. D'') Volcano plots representing differentially expressed genes ($q < 0.05$; $\log_2$ fold-difference >1.5) between PDGFRA^{Hi} and PDGFRA^{Lo} cells in antrum (left) and corpus (right). Selected genes are shown.

E) Relative expression of secreted niche factor mRNAs in purified mesenchymal cell populations, selected from a full set of BMP, WNT, FGF and EGF pathway agonists and antagonists. The heatmap is prepared from normalized rlog counts from DEseq2. Duplicate RNA-seq libraries are represented.

Figure 3

A) On the left: clustering of populations by UMAP plot of RNA profiles from 34,445 single cells proceeding from corpus (20,624) and antrum (13,821) mesenchyme. On the right: dot-plot representing relative expression of known stromal cell markers in cell clusters identified by scRNA-seq. Circle sizes represent the percentage of cells expressing a gene within the population, fill colors represent normalized average expression per population.

B) MetaNeighbour AUROC analysis shows extremely high similarity between corresponding mesenchymal populations from antrum and corpus except for PDGFRA^{Hi} and PDGFRA^{Lo} sub-populations identified by scRNAseq clustering.

C) On the left: UMAP projection of subset *Pdgfra*-expressing cells and identification of discrete sub-populations based on clustering and Pdgfra expression levels. On the right: violin plots representing the expression of *Pdgfra* and *Cd34* in the identified populations and comparison with SI populations (corpus in blue, antrum in red, SI in green). Corpus PDGFRA^{+} present three separated clusters, one of PDGFRA^{Hi} and two of PDGFRA^{Lo} cells (CorpLo1 and CorpLo2). Antral PDGFRA^{+} clusters are more closely related compared to corpus ones. We identified three antral sub-populations: PDGFRA^{Hi}, PDGFRA^{Int} and PDGFRA^{Lo}.

D) Gene markers differentially expressed among the six PDGFRA^{+} mesenchymal cell types ($p < 0.01$, average $\log_2$ fold change >1). 100 top marker genes of each population are available in Table S2.

E) Gene expression of *Bmp7* and *Nrg1* in the identified populations and comparison with SI populations (corpus in blue, antrum in red, SI in green). PDGFRA^{Int} show expression levels of those genes comparable to antral PDGFRA^{Hi}. *Nrg1* expression in corpus and SI is significantly lower than in antrum.

F) Relative expression of marker genes from the five PDGFRA^{+} sub-populations identified by scRNA-seq. Circle sizes represent the percentage of cells expressing a gene within the population, fill colors represent normalized average expression per population. PDGFRA^{Int} population shows an intermediate gene expression pattern.

G) Gene expression of *Grem1* and *Rspo3* in the identified populations and comparison with SI populations (corpus in blue, antrum in red, SI in green). *Grem1* and *Rspo3* expression is confined in PDGFRA^{Lo} cells and it is generally lower in the gastric mesenchymal cells compared to SI.

Figure 4

A) On the left: UMAP plot of subset gastric PDGFRA^{Hi}-SEMFs cells showing a clear separation between cells proceeding from corpus (blue) and antrum (orange-red), and a neat split of antral PDGFRA^{Hi} into two different sub-populations. On the right: projection of *Fgf7, Nrg1, Bmp3* and *Ctgf* single-cell transcript density onto PDGFRA^{Hi} UMAP plot, which expression defines three major populations.

B) Relative expression of marker genes from the three PDGFRA^{Hi} sub-populations identified by scRNA-seq. Circle sizes represent the percentage of cells expressing a gene within the population, fill colors represent normalized average expression per population. Antral sub-populations clearly show different gene expression patterns between *Bmp3*$^{+}$ and *Fgf7*$^{+}$*;Nrg1*$^{+}$ sub-populations, while corpus PDGFRA^{Hi} population shows similarities to antral *Bmp3*$^{+}$ one.

C) RNA *in situ* hybridization on antrum sections localizes *Fgf7* and *Nrg1* PDGFRA^{Hi} expressing cells near the “pit” of the glands, while *Bmp3* and *Ctgf* expressing cells are located in the lower half of the glands, corresponding to the proliferative zone of epithelial cells. Images represent several fields examined in three independent experiments. Scale bar 50um. In the middle,

heatmap representation of probe signal derived from quantification of fluorescence along 16-25 individual glands. On the right, schematic representation of antral PDGFRA^{Hi} sub-populations distribution relatively to epithelial cells.

D) Co-culture of antral glands with unfractionated antral PDGFRA^{Hi} in Matrigel. PDGFRA^{Hi} cells are not able to induce antrum organoid formation in absence of rNOGGIN and RSPO1.

E) Antral glands treated with recombinant FGF7 in addition to complete media (ENRW) show an increase in budding structures (quantification in Figure S4D).

F) Clustering of populations by UMAP plot of RNA profiles from 9,480 single cells proceeding from WT (3,885) and *Fgf7-KO* (5,595) epithelium. Cells isolated from WT and *Fgf7-KO* antrum show no significant difference in cell population ratios. Despite the over-lap between Foveolar cells is not absolute, no significant differences were observed in gene expression (see Table S4).

Figure 5

A) UMAP plot of subset gastric PDGFRA^{Lo} cells showing five distinct populations: previously identified *Pdgfra^{Int}*, AntLo and CorpLo1 populations, with the addition of two sub-populations derived from CorpLo: CorpLo2 and CorpLo3.

B) Projection of *Grem1* and *Ctgf* single-cell transcripts density onto the PDGFRA^{Lo} UMAP map. CorpLo1, CorpLo2 and AntLo populations present the highest expression of both genes.

C) RNA *in situ* hybridization on antrum sections localizes *Grem1* and *Ctgf* transcripts near the gland base, in the area corresponding to PDGFRA^{Lo} expressing cells and near the epithelial stem cell zone. Images represent several fields examined in three independent experiments. Scale bar 50um. On the right, heatmap representation of probe signal derived from quantification of fluorescence along 35-39 individual glands.

D) Schematic representation of antral PDGFRA^{Lo} populations distribution relatively to epithelial cells. Two distinct populations of PDGFRA^{Lo} cells are present in the gastric mesenchyme, and *Grem1/Ctgf* expressing population are situated below the gland bottom in the antrum.

E) Projection of *Cd55* single-cell transcript density onto the PDGFRA^{Lo} UMAP map. CorpLo1, CorpLo2 and AntLo populations present the highest expression of the gene.

F) GFP flow cytometry separates PDGFRA^{Hi} from PDGFRA^{Lo} cells from whole mesenchyme isolated from antrum (top). Staining with Cd55 antibody allows the separation of CD55^{+} and CD55^{-} fractions of PDGFRA^{Lo} cells (bottom).

G) Co-culture of antral glands with CD55^{+} PDGFRA^{Lo} or CD55^{-} PDGFRA^{Lo} cells in Matrigel. CD55^{+} PDGFRA^{Lo} cells induce antrum organoid formation in absence of recombinant factors.

H) Organoid formation quantification of *small intestinal crypts (SI), antrum (A) or corpus (C) glands co-cultured with trophocytes from different gastrointestinal regions in Matrigel (n=3-10). Crypts co-cultured of with either antrum or corpus trophocytes show no growth, while antrum and corpus glands show no significant changes in their growth independently from the trophocytes origin. Bars represent mean ± SEM values. Significance of differences was determined by one-way ANOVA. **p<0.01; ns = not significant. If not indicated, no significant difference is observed.*

I) Schematic representation of all the identified antral PDGFRA^{+} cell subpopulations in relation to the epithelium.

SUPPLEMENTARY FIGURES

Figure S1

A) Whole-mount 3D rendering of corpus (left) and antrum (right) glands stained with laminin (yellow) to mark basal lamina, highlighting epithelium-mesenchyme interface and gland pits. Scale bar 50um.

B) Whole-mount 3D rendering of antrum (left) and corpus (right) glands highlighting capillaries (red) organization. Corpus shows an extended net of capillaries, branching along the whole gland length, while antrum capillaries are mainly connected below the gland bases and at their pits. Arterioles with bigger diameters feed the capillaries in both regions. Laminin immunostaining in yellow, CD31 in red. Scale bar 50um.

C) Whole-mount 3D rendering of antrum glands in *Pdgfra*^{H2BeGFP} mouse showing the blood vessel (yellow) organization PDGFRA^{+} distribution (green) across multiple glands. Scale bar 50um.

D) Grayscale image of GFP signal of gland cross-sections represented in Figure 1D to appreciate differential GFP signal in PDGFRA^{Hi} (green arrow heads) and PDGFRA^{Lo} (green arrow) cells. Scale bar 50um.

E) Whole-mount 3D rendering of corpus (top) and antrum (bottom) glands in *Pdgfra*^{H2BeGFP} mice. Laminin (yellow) marks the basal lamina. PDGFRA^{Hi} (arrow heads) and PDGFRA^{Lo} (arrow) are indicated. On the right: quantification of GFP signal distribution along the glands in corpus (top) and antrum (bottom) shows high concentration of GFP signal at corpus gland base and antral pit. Scale bar 50um.

F) Extracted frames from video 1 (left, corpus) and 2 (right, antrum) showing *Pdgfra*$^{+}$ cells (green) in *PdgfraCre*$^{ERT2+}$*;Rosa26*$^{mT/mG}$ mouse. *Pdgfra*$^{+}$ cells cover the basal side of the epithelium with their extensions.

G) GFP flow cytometry separates PDGFRA^{Hi} from PDGFRA^{Lo} cells from whole mesenchyme isolated from corpus (top) and antrum (bottom).

H) Co-culture of gastric glands with PDGFRA^{Lo} cells isolated from the same region in Matrigel (C corpus, A antrum). PDGFRA^{Lo} cells from corpus and antrum are able to induce organoid formation from glands proceeding from the same region in absence of rNOGGIN and RSPO1.

I) Quantification of organoid formation from experiments represented in figures 1G and S1H (n = 3-6). Bars represent mean ± SEM values. Significance of differences was determined by one-way ANOVA. ***$p < 0.001$; ns = not significant.

Figure S2

A) qRT-PCR analysis of antrum and corpus epithelial cell markers, relative to *Gapdh*. Organoids were cultured in complete media (ENRW) for 4 days. qRT-PCR confirm differential levels of region-specific marker genes between corpus (blue) and antrum (orange) organoids.

B) Quantification of organoid growth in different media conditions. Dots indicate factor concentration: full, half or no factor (empty dot). Factors: E: recombinant EGF; N: recombinant NOGGIN; R: RSPO1 conditioned media; W: AFAMIN/WNT3A conditioned media. Bars represent mean ± SEM values (n = 4-8). Significance of differences was determined by one-way ANOVA comparing each condition with control organoids growth in full concentration of all factors (ENRW). *p<0.05; **p<0.01; ****p<0.0001.

C) Principal components analysis (PCA) plot of duplicate bulk RNA-seq samples of the indicated cell types shows high concordance between replicates. SI: small intestine; C: corpus; A: antrum; Hi: PDGFRA^{Hi}; Lo: PDGFRA^{Lo}.

D) Volcano plot representing differentially expressed genes ($q < 0.05$; $\log_2$ fold-difference >1.5) between corpus and small intestine (SI) PDGFRA^{Hi} cells. Selected genes are shown. Venn diagram represents differentially expressed gene numbers.

E) Volcano plot representing differentially expressed genes ($q < 0.05$; $\log_2$ fold-difference >1.5) between PDGFRA^{Hi} and PDGFRA^{Lo} cells in small intestine. Selected genes are shown.

Figure S3

A) Violin plots representing single cell RNA-sequencing samples data quality.

B) On the left: clustering of all mesenchymal populations by UMAP plot of RNA profiles from 34,445 single cells proceeding from corpus (20,624, blue) and antrum (13,821, orange-red) grouped by region of origin, showing overlap between all major populations except Pdgfra-expressing cells. On the right: UMAP plot of sub-set *Pdgfra*$^+$ cells showing a clear separation between cells proceeding from corpus and antrum (top) and projection of *Pdgfra* single-cell transcripts density onto the *Pdgfra*$^+$ UMAP map.

C) Relative expression of selected genes from BMP, WNT, FGF and EGF pathways from all mesenchymal populations identified by scRNA-seq. Circle sizes represent the percentage of cells expressing a gene within the population, fill colors represent normalized average expression per population. PDGFRA$^+$ cells are the major populations expressing genes belonging to these pathways.

D) On the left: gene expression of PDGFRA^{Lo} markers *Sfrp1, Fbln1* and *Eln* of gastric PDGFRA^{+} subpopulations (left) and PDGFRA^{Hi} and PDGFRA^{Lo} from small intestine (right). Gastric PDGFRA^{Lo} populations show a similar gene expression pattern to PDGFRA^{Lo} cells from small intestine. On the right: gene expression of *Bmp2, Bmp4* and *Bmp5* of gastric PDGFRA^{+} subpopulations (left) and PDGFRA^{Hi} and PDGFRA^{Lo} from small intestine (right). PDGFRA^{Int} population shows an intermediate gene expression pattern.

E) Relative expression of selected genes from BMP, Wnt, FGF and EGF pathways from gastric (top) and SI (bottom) PDGFRA^{+} subpopulations identified by scRNA-seq. Circle sizes represent the percentage of cells expressing a gene within the population, fill colors represent normalized average expression per population. PDGFRA^{Int} population gene expression pattern is intermediate between PDGFRA^{Lo} and PDGFRA^{Hi} ones and gastric PDGFRA^{+} cells present higher BMP tone compared to SI.

Figure S4

A) UMAP plot of subset gastric PDGFRA^{Hi} cells identifying three separated subpopulations, homogeneous corpus PDGFRA^{Hi}, antrum *Bmp3*$^{+}$ and antrum *Fgf7*$^{+}$;*Nrg1*$^{+}$ sub-populations. On the right, projection of *Bmp7, Bmp5* and *Bmp4* single-cell transcripts density onto the PDGFRA^{Hi} UMAP map shows that genes for BMP ligands are homogenously expressed among sub-populations.

B) Organoid formation quantification to assess BMP3 and CTGF effect on antral organoids growth. Antral organoids were treated with recombinant BMP3 or recombinant CTGF in addition to media with reduced RSPO1 and AFAMIN/Wnt3a (2%) without NOGGIN. rBMP3 and rCTGF are not able to replace NOGGIN in the induction of organoid growth *in vitro* (n=3). Bars represent mean ± SEM values. Significance of differences was determined by one-way ANOVA. **p<0.01; ***p<0.001; ****p < 0.0001.

C) Organoid formation quantification of gastric glands co-culture with same-region PDGFRA^{Hi} in Matrigel (n=7-10). PDGFRA^{Hi} cells do not induce organoid formation in absence of recombinant factors. Bars represent mean ± SEM values. Significance of differences was determined by one-way ANOVA. ****p < 0.0001; ns = not significant.

D) Quantification of budding structures and total organoid formation upon treatment with recombinant FGF7, in addition to complete media (ENRW). FGF7 treatment induces an increase in budding structures and no significant changes in organoid total number (n=8). Bars represent mean ± SEM values. Significance of differences was determined by t-student statistical analysis. ****p < 0.0001; ns = not significant.

E) On the top: Schematic representation of the newly generated *Fgf7*$^{fl/fl}$ allele. On the bottom: agarose gel showing genotyping PCR on mesenchymal cells isolated from WT (*Fgf7*$^{+/+}$) or *Pdgfra*$^{Cre(ER-T2)}$*;Fgf7*$^{fl/fl}$ with or without Cre activation (2 consecutive i.p. injections of 2 mg tamoxifen). Antrum section of *Pdgfra*$^{Cre(ER-T2)}$*;Rosa26*$^{LSL-tdTomato}$ mouse showing *Cre* activity mainly in PDGFRA^{Hi} cells upon tamoxifen injection.

F) Immunostainings of antrum from WT and *Pdgfra*$^{Cre(ER-T2)}$*;Fgf7*$^{fl/fl}$ mice. *Fgf7* deficiency shows no impact on MUC5AC production and secretion, number or localization of GASTRIN and SST producing cells. Scale bar 50um.

Figure S5

A) UMAP plot of sub-set gastric PDGFRA^{Lo} cells showing a clear separation of cells from corpus (blue) and antrum (orange-red), except for few antral cells that cluster with CorpLo1.

B) Relative expression of marker genes from the five PDGFRA^{Lo} subpopulations identified by scRNA-seq. Circle sizes represent the percentage of cells expressing a gene within the population, fill colors represent normalized average expression per population. CorpLo3 share similar gene expression with previously identified antral PDGFRA^{Int} population. Clusters AntLo, CorpLo1 and CorpLo2 present similarities in their gene expression patterns.

C) Projection of *Grem1*, *Ctgf* and *Grem1-Ctgf* co-expression single-cell transcript density onto the UMAP map. *Grem1* and *Ctgf* are expressed by clusters AntLo, Corp1 and Corp2, and rarely co-expressed.

D) Projection of *Bmp5, Bmp7, Wnt4* and *Rspo3* single-cell transcript density onto the UMAP map. CorpLo3 and PDGFRA^{Int} clusters are the main populations expressing BMP ligands and non-canonical Wnt among PDGFRA^{Lo} populations, while AntLo, Corp1 and Corp2 clusters express *Rspo3*.

E) GFP flow cytometry separates PDGFRA^{Hi} from PDGFRA^{Lo} cells from whole mesenchyme isolated from corpus (left). Staining with CD55 antibody allows the separation of CD55^{+} and CD55^{-} fractions of PDGFRA^{Lo} cells (right).

F) Organoid formation quantification of antral glands co-cultured with CD55^{+} and CD55^{-} fractions of antral PDGFRA^{Lo} in Matrigel (n=12). Co-culture of antral glands with PDGFRA^{Lo} CD55^{+} cells show no difference with complete media treatment (ENRW), while PDGFRA^{Lo} CD55^{+} are not able to induce organoid formation. Bars represent mean ± SEM values. Significance of differences was determined by one-way ANOVA. ***$p<0.001$; ****$p < 0.0001$; ns = not significant.

G) Co-culture of corpus glands with $CD55^{+}$ $PDGFRA^{Lo}$ or $CD55^{-}$ $PDGFRA^{Lo}$ cells in Matrigel (left) and quantification of organoid formation (right). As observed for the antrum, $CD55^{+}$ $PDGFRA^{Lo}$ cells induce corpus organoid formation in absence of recombinant factors, while $CD55^{-}$ cells are incapable. n=4; *$p<0.05$; ns = not significant.

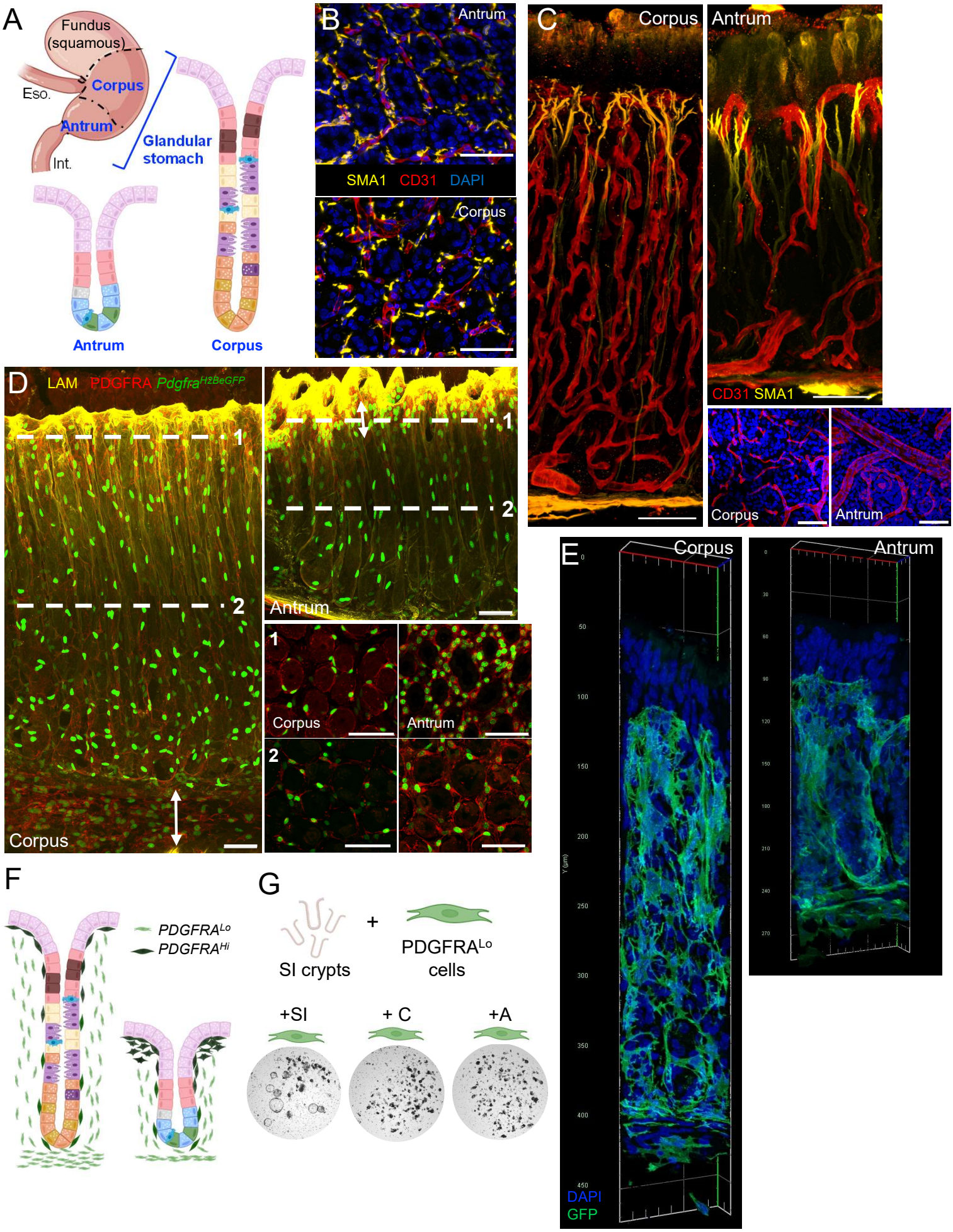
A
Fundus (squamous)
Eso.
Corpus
Antrum
Int.
Glandular stomach
Antrum
Corpus
B
Antrum
SMA1 CD31 DAPI
Corpus
C
Corpus
Antrum
CD31 SMA1
Corpus
Antrum
D
LAM PDGFRA Pdgfra H2BeGFP
1
2
Corpus
1
2
Antrum
1
Corpus
Antrum
2
E
Corpus
Antrum
DAPI
GFP
F
PDGFRA Lo
PDGFRA Hi
G
SI crypts
+
PDGFRA Lo cells
+SI
+ C
+A

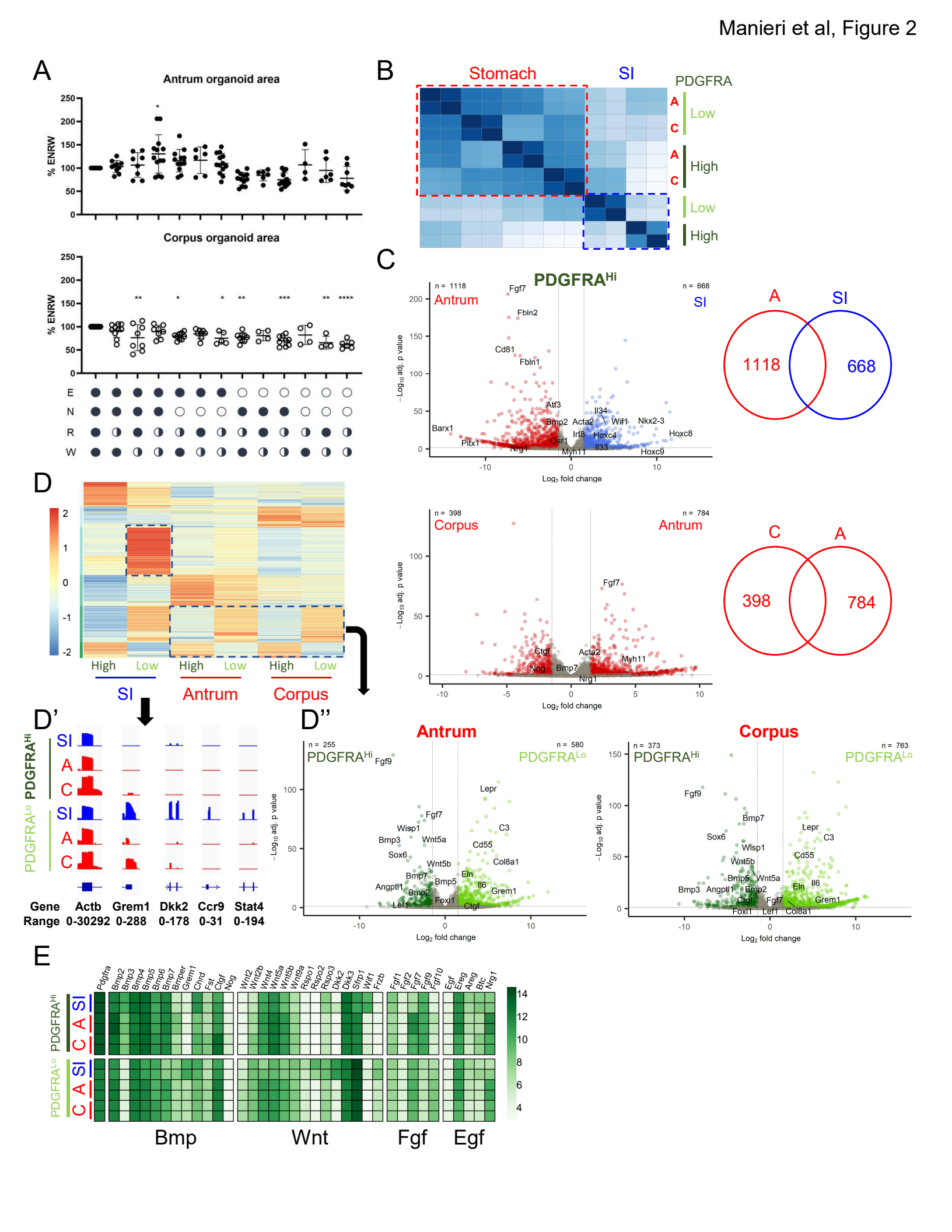
A
Antrum organoid area
% ENRW
Corpus organoid area
E
N
R
W
B
Stomach
SI
PDGFRA
A
C
Low
High
C
PDGFRA^Hi
n = 1118
Antrum
n = 668
SI
Log2 fold change
1118
668
n = 398
Corpus
n = 784
Antrum
398
784
D
High
Low
SI
Antrum
Corpus
D'
PDGFRA^Hi
PDGFRA^Lo
Gene Range
Actb 0-30292
Grem1 0-288
Dkk2 0-178
Ccr9 0-31
Stat4 0-194
D''
Antrum
n = 255
PDGFRA^Hi
n = 580
PDGFRA^Lo
Corpus
n = 373
PDGFRA^Hi
n = 763
PDGFRA^Lo
E
Bmp
Wnt
Fgf
Egf

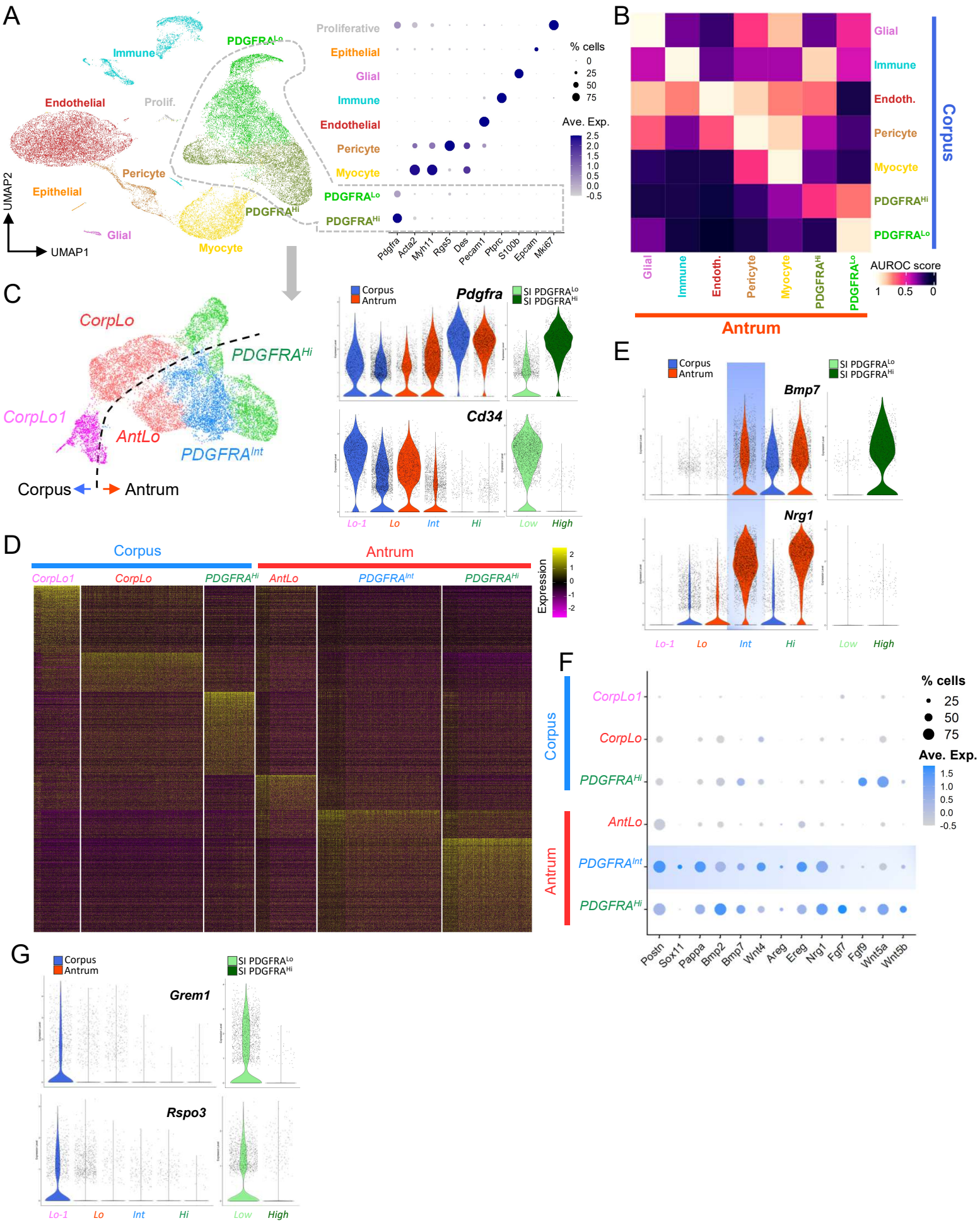
A
Immune
PDGFRA^Lo
Endothelial
Prolif.
Pericyte
Epithelial
PDGFRA^Hi
Glial
Myocyte
UMAP2
UMAP1
Proliferative
Epithelial
Glial
Immune
Endothelial
Pericyte
Myocyte
PDGFRA^Lo
PDGFRA^Hi
Pdgfra
Acta2
Myh11
Rgs5
Des
Pecam1
Ptprc
S100b
Epcam
Mki67
% cells
0
25
50
75
Ave. Exp.
2.5
2.0
1.5
1.0
0.5
0.0
-0.5
B
Glial
Immune
Endoth.
Pericyte
Myocyte
PDGFRA^Hi
PDGFRA^Lo
Corpus
AUROC score
1
0.5
0
Antrum
C
CorpLo
PDGFRA^Hi
CorpLo1
AntLo
PDGFRA^Int
Corpus
Antrum
Corpus
Antrum
Pdgfra
SI PDGFRA^Lo
SI PDGFRA^Hi
Cd34
Lo-1
Lo
Int
Hi
Low
High
D
Corpus
Antrum
CorpLo1
CorpLo
PDGFRA^Hi
AntLo
PDGFRA^Int
PDGFRA^Hi
Expression
2
1
0
-1
-2
E
Corpus
Antrum
SI PDGFRA^Lo
SI PDGFRA^Hi
Bmp7
Nrg1
Lo-1
Lo
Int
Hi
Low
High
F
Corpus
Antrum
CorpLo1
CorpLo
PDGFRA^Hi
AntLo
PDGFRA^Int
PDGFRA^Hi
% cells
25
50
75
Ave. Exp.
1.5
1.0
0.5
0.0
-0.5
Postn
Sox11
Pappa
Bmp2
Bmp7
Wnt4
Areg
Ereg
Nrg1
Fgf7
Fgf9
Wnt5a
Wnt5b
G
Corpus
Antrum
SI PDGFRA^Lo
SI PDGFRA^Hi
Grem1
Rspo3
Lo-1
Lo
Int
Hi
Low
High

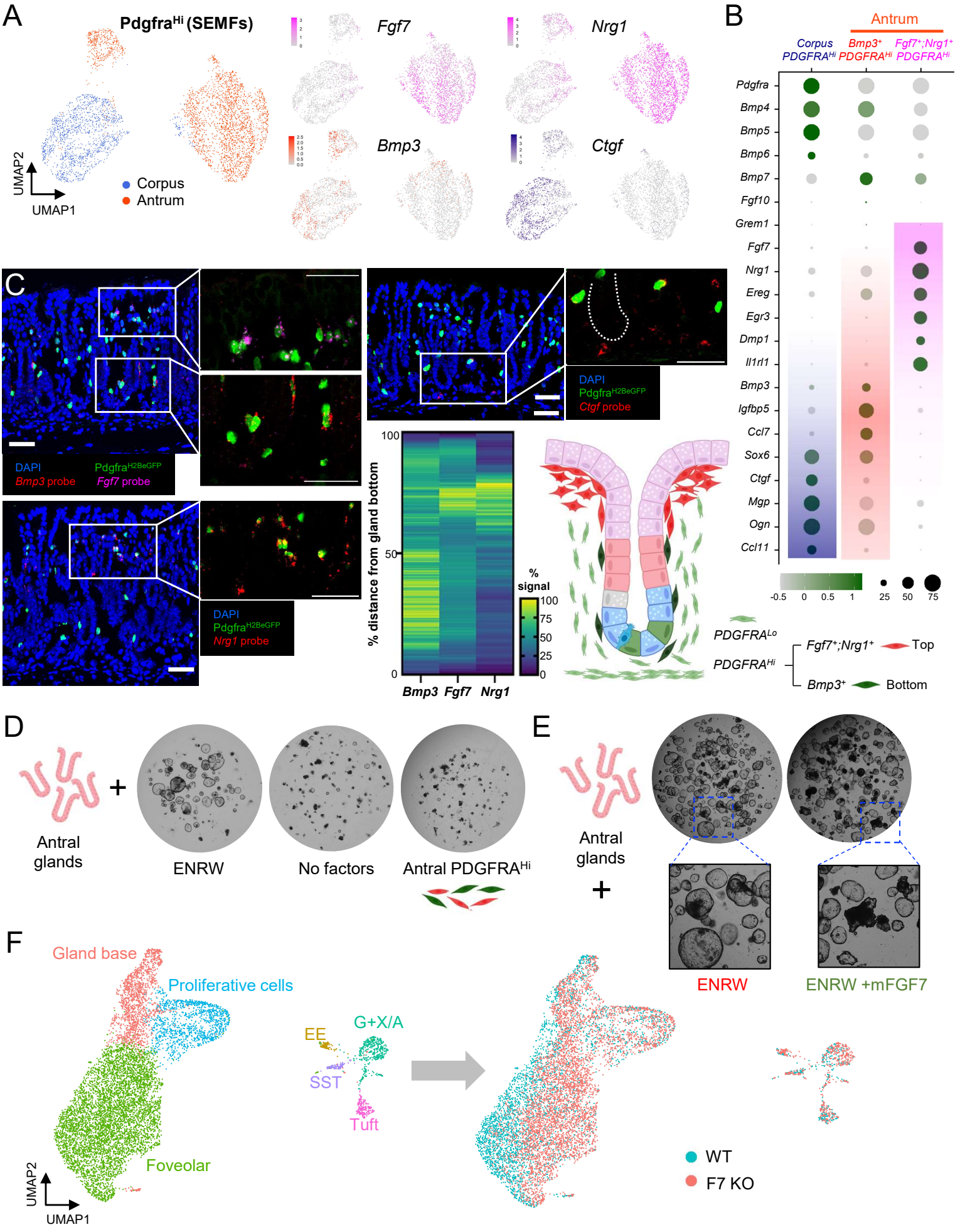
A
PdgfraHi (SEMFs)
Fgf7
Nrg1
Bmp3
Ctgf
UMAP2
UMAP1
Corpus
Antrum
B
Antrum
Corpus PDGFRAHi
Bmp3+ PDGFRAHi
Fgf7+;Nrg1+ PDGFRAHi
Pdgfra
Bmp4
Bmp5
Bmp6
Bmp7
Fgf10
Grem1
Fgf7
Nrg1
Ereg
Egr3
Dmp1
Il1rl1
Bmp3
Igfbp5
Ccl7
Sox6
Ctgf
Mgp
Ogn
Ccl11
-0.5 0 0.5 1
25 50 75
C
DAPI
Bmp3 probe
PdgfraH2BeGFP
Fgf7 probe
DAPI
PdgfraH2BeGFP
Nrg1 probe
DAPI
PdgfraH2BeGFP
Ctgf probe
% distance from gland bottom
100
50
0
Bmp3 Fgf7 Nrg1
% signal
100
75
50
25
0
PDGFRALo
PDGFRAHi
Fgf7+;Nrg1+
Top
Bmp3+
Bottom
D
Antral glands
ENRW
No factors
Antral PDGFRAHi
E
Antral glands
ENRW
ENRW +mFGF7
F
Gland base
Proliferative cells
Foveolar
UMAP2
UMAP1
EE
G+X/A
SST
Tuft
WT
F7 KO

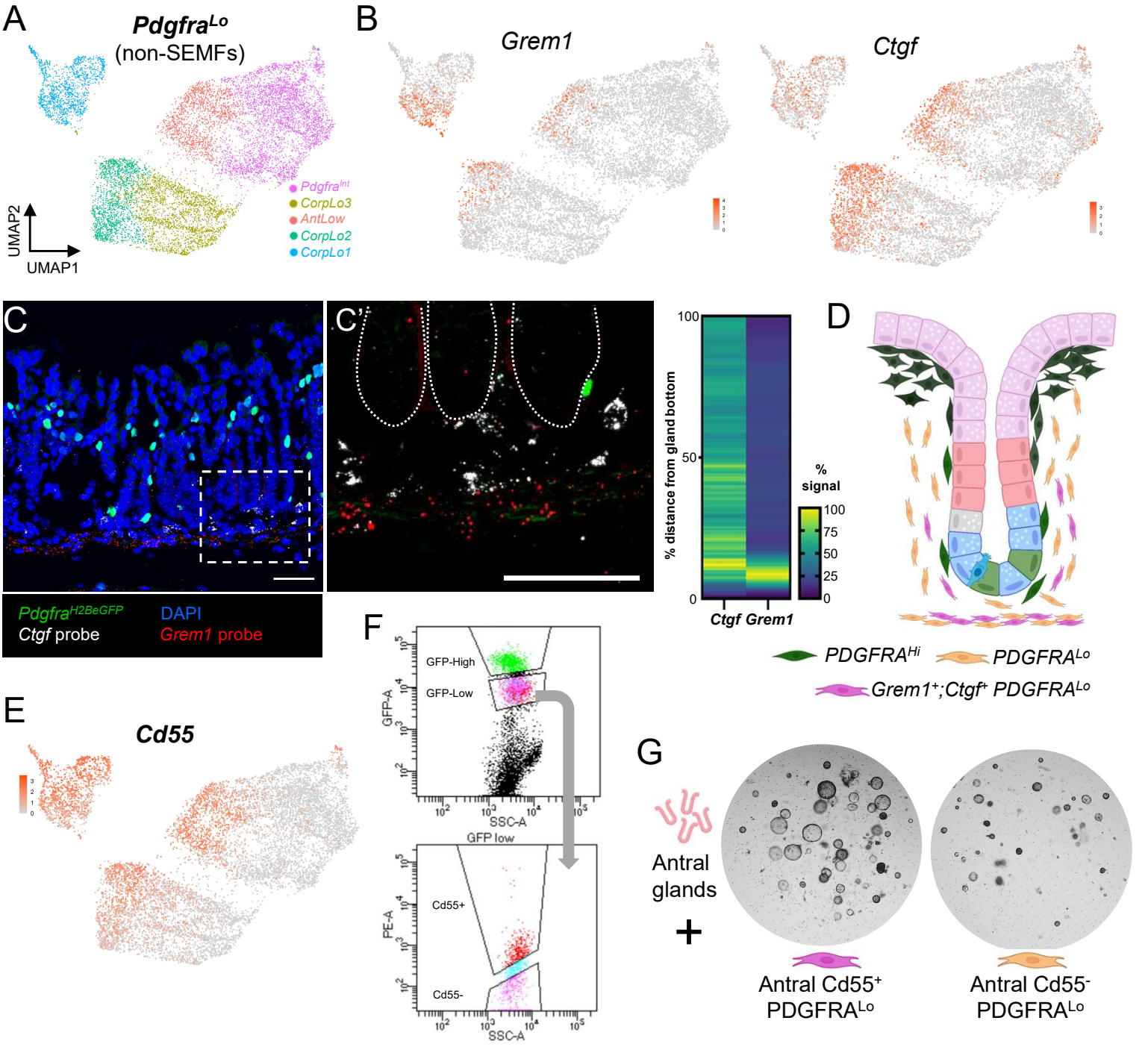
A
Pdgfra^Lo
(non-SEMFs)
Pdgfra^Int
CorpLo3
AntLow
CorpLo2
CorpLo1
UMAP2
UMAP1
B
Grem1
Ctgf
C
C'
Pdgfra^H2BeGFP
DAPI
Ctgf probe
Grem1 probe
% distance from gland bottom
100
50
0
Ctgf Grem1
% signal
100
75
50
25
0
D
PDGFRA^Hi
PDGFRA^Lo
Grem1+;Ctgf+ PDGFRA^Lo
E
Cd55
F
GFP-High
GFP-Low
GFP-A
SSC-A
GFP low
Cd55+
Cd55-
PE-A
SSC-A
G
Antral glands
+
Antral Cd55+ PDGFRA^Lo
Antral Cd55- PDGFRA^Lo

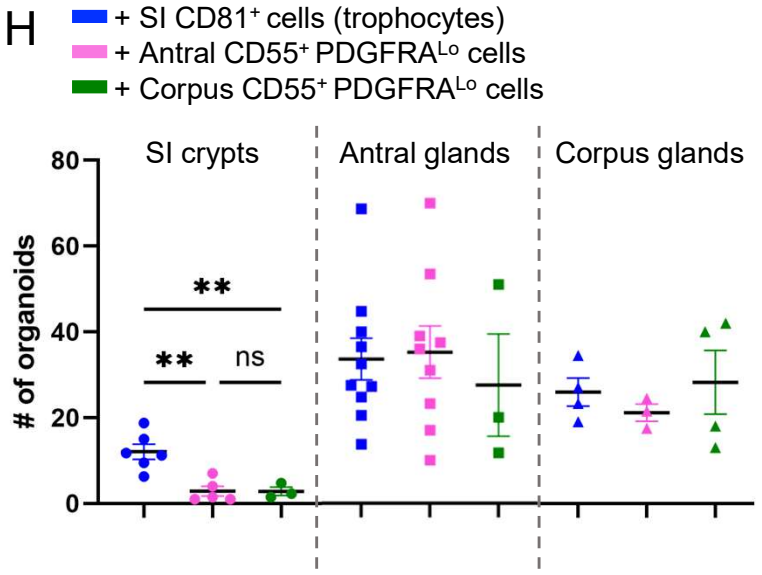
H
+ SI CD81+ cells (trophocytes)
+ Antral CD55+ PDGFRA^Lo cells
+ Corpus CD55+ PDGFRA^Lo cells
SI crypts
Antral glands
Corpus glands
# of organoids
80
60
40
20
0
**
**
ns

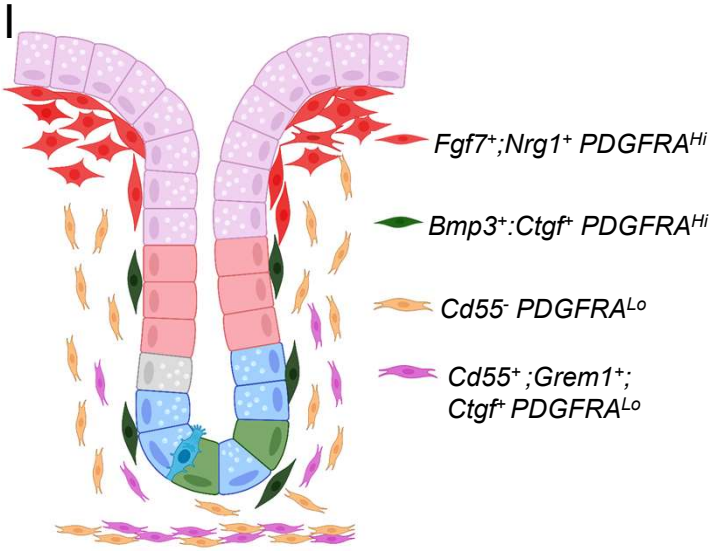
I
Fgf7+;Nrg1+ PDGFRA^Hi
Bmp3+:Ctgf+ PDGFRA^Hi
Cd55- PDGFRA^Lo
Cd55+ ;Grem1+;
Ctgf+ PDGFRA^Lo